Meccanica
https://doi.org/10.1007/s11012-024-01774-6

RESEARCH

Correlation and modal analysis techniques for the study of the VIV response of a twin-box deck based on 3D LES simulations

Antonio J. Álvarez · Félix Nieto

Received: 5 February 2024 / Accepted: 27 February 2024

Abstract Twin-box decks are prone to vortex-induced vibration (VIV) at moderate wind speeds, and previous studies have shown a complex interplay between the flow and the two parallel box girders. OpenFOAM is used to model the aerodynamic and aeroelastic responses of the twin-box deck of the Stonecutters Bridge by means of 3D LES simulations. Two cases are thoroughly analysed under smooth incoming flow: (i) static deck and ii) heave peak amplitude response at VIV excitation. The computational data provided by the CFD simulations have been exploited aiming at better understanding the complex aerodynamic and aeroelastic phenomena taking place. First, spanwise correlation analyses are applied to understand the level of organisation of the forcing flow actions, and identify the regions of the deck affected by different flow structures. Second, three different mode decomposition techniques (POD, SPOD and DMD) are applied to the time-dependent pressure distributions, revealing the pivotal role played by the leeward box in the twin-box deck response under wind action. The modal analyses are of utmost interest in the development of Reduced Order Models (ROM) for the VIV response of twin-box long-span bridges.

A. J. Álvarez (✉) · F. Nieto
CITEEC, University of A Coruña, A Coruña, Spain
e-mail: antonio.jose.alvarez@udc.es

F. Nieto
e-mail: felix.nieto@udc.es

Keywords VIV · 3D LES · Correlations · POD · SPOD · DMD

1 Introduction

Fluid mechanics is present in almost every aspect of our daily life: from opening a water tap up to launching a rocket to deliver an earth observation satellite, the ability of engineers to tackle challenging flow problems is put to the test. Nowadays, we are witnessing a time in which we can even grasp some of the complex features associated with environmental flows and the effects on the built environment. In the field of wind engineering applications, some challenges should be remarked: the large extension of the flow domain of interest, the high Reynolds number, the turbulent nature of the flow, the development of boundary and shear layers when the flow interacts with solid surfaces, the complexity linked to flow separation, reattachment, impingement and shedding of vortices, and eventually fluid–structure interaction episodes giving rise to aeroelastic phenomena that might eventually end in unstable structural responses. Only recently computational methods have been able to contribute to a better understanding of these phenomena, complementing the traditionally established wind tunnel testing approach. It is therefore crucial to outline where computational modelling practice stands nowadays in order to understand the challenges

Published online: 13 April 2024

that computational wind engineers will be facing in the years to come.

From a structural design perspective, field measurements are of limited interest in applied wind engineering design, as the priority should be to avoid wind-induced damages or service problems at the project definition stage. Therefore, during the twentieth-century, experimental methods, in particular wind tunnel testing at reduced geometrical scales, have been favoured as the standard tool to address wind effects on structures. However, as computational fluid mechanics gained maturity at the end of the past century, and computational power dramatically increased, engineers acquired an additional tool to address fluid mechanics problems, to a large extend complementary to wind tunnel testing. Computational fluid dynamics (CFD) now provides, not only local values for flow properties, similar to experimental instrumentation, but a complete description of the flow in space and time. There still exist limitations for computational approaches, such as the associated computational burden, uncertainties in turbulence models, selection of values for numerical parameters and boundary conditions definition, the difficulty in addressing problems with Reynolds numbers similar to real scale applications, or the complexity of tackling certain problems such as transition from laminar to turbulent regimes. A comprehensive review about the state of the art in CFD applications in wind engineering can be found in Blocken [5].

Turning now the focus towards long-span bridge engineering applications, one should take into consideration some specific features that delimitate what might be feasible and meaningful among the available CFD approaches. The fundamental characteristics to highlight are: (i) the extreme flexibility and low mechanical damping of this structural typology that explains the susceptibility to aeroelastic phenomena such as flutter; and (ii) the long length of the deck, which can reach several kilometres, along with the height of the towers, frequently of more than 100 m, which even prevent the development of a reduced scale CFD model of the full bridge. Consequently, the standard approach in computational fluid dynamics has been to replicate wind tunnel reduced scale sectional model tests, with sizes and Reynolds numbers feasible for CFD models. These wind tunnel tests are the source of the experimental data used for the fundamental validation of the numerical results.

The work covered by this article aims at providing a glimpse of what can be done today in the field of wind-induced effects in long-span bridges, focusing on pre-processing and post-processing capabilities using the open-source solver OpenFOAM. In fact, at postprocessing level, in this article the focus is put on correlation and modal analysis of the pressure distributions. The application case adopted is the bare deck of the Stonecutters Bridge, a twin-box deck cable-stayed bridge built in Hong-Kong (P.R. of China) in 2009. The computational approach reported herein is based upon a 3D LES (Large Eddy Simulation) model and incoming smooth flow, which extends previous studies conducted by the authors [2]. Of course, OpenFOAM has been previously adopted in CFD studies of long-span bridges, such as in Fransos and Bruno [10], Sarkic et al. [24], or de Miranda et al. [9], to point out just a few.

As a final introductory remark, the possibilities that CFD simulations enable in the frame of data-based design should be highlighted [15]. On the one hand, the huge amount of information available in computational models is a very valuable source of data on its own right; and on the other hand, the ability of running multiple CFD models in parallel, taking advantage of HPC (High Performance Computing) technology, allows completing parametric studies, evaluating the samples of a surrogate model or providing data for AI (Artificial Intelligence) applications in a feasible timeframe. Open-source solvers such as OpenFOAM are therefore instrumental for data-enabled design.

The paper is organized as follows: first, a section introducing the formulation for calculating the correlation coefficients and the different mode decomposition approaches used in this piece of research is presented. In Sect. 3, the adopted computational model is described and the application case is introduced. Afterwards, two sets of computational results are reported and analysed, organized in two sections: one focusing on the correlation coefficients of the force coefficients and pressure coefficients over the twin-box deck surfaces (Sect. 4), and another presenting the mode shapes and their characteristics for the different mode decomposition techniques considered (Sect. 5). Finally, a section summarizing the main findings and fundamental remarks is included as a closure for this research.

2 Formulation

2.1 Fundamental aerodynamic parameters and dynamic properties

The force coefficients represent the non-dimensional aerodynamic force components per unit of span length acting on the body under study. Sub-indexes d, l and m stand for the drag, lift and moment components. They are evaluated as:

$$C_d = \frac{F_d}{\frac{1}{2}\rho U^2 C}, C_l = \frac{F_l}{\frac{1}{2}\rho U^2 C}, C_m = \frac{M}{\frac{1}{2}\rho U^2 C^2}, \tag{1}$$

where F_d represents the drag force pers unit of span length, F_l is the lift force per unit of span length and M is the centroid-axis moment per unit of span length (sign conventions are provided in Fig. 1). The geometry under study is the Stonecutters twin-box bridge deck, without considering the transversal beams connecting the two boxes. Additionally, in Eq. 1, C is the the breadth of a single box.

The Strouhal number, which is a non-dimensional parameter related with the frequency of the periodic aerodynamic excitation due to vortex shedding, is defined as:

$$St = \frac{fD}{U}, \tag{2}$$

being f the dominant frequency in the lift force spectrum and D is the height of the deck (Fig. 1).

The pressure coefficient at any location over the surface of the body is evaluated as follows, where p is the time-dependent pressure at the considered location:

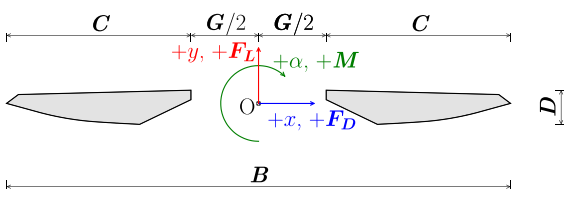

Fig. 1 Sign convention (B stands for the overall width of the deck, C is the width of a single box, G is the gap distance between boxes, O is the reference point for the forces and moments)

$$C_p = \frac{p}{\frac{1}{2}\rho U^2}. \tag{3}$$

The free decaying simulations were conducted for the heave degree of freedom (y axis in Fig. 1). Those simulations are characterized by the natural frequency and damping factor of the one degree of freedom dynamical system. The damping is given in its non-dimensional form, Scruton number, whose equation is presented hereunder:

$$Sc = \frac{4\pi m\varsigma}{\rho LD}, \tag{4}$$

where m is the mass of the system, ς is the relative damping of the system and L is the spanwise length.

2.2 Spanwise correlation

The correlation coefficient is a statistical parameter that provides values between -1 and 1, aiming at quantifying the strength of the interdependency between two variables. The value of zero means that the two variables are uncorrelated, and for the case of linear and Gaussian stochastic processes this also indicates independence. Moreover, the correlation coefficient provides information about the phase lag between the two variables under study: when two variables with pure sinusoidal time-histories are considered, the correlation coefficient is equal to $\cos\phi$, being ϕ the phase lag between the two time-histories. For a generic time-history, containing multiple frequencies, the correlation coefficient is the summation of the cosines of the phase lags of the different frequency components. Correlation also has a physical meaning in fluid–structure interaction phenomena since, according to Ricciardelli [21], the lower the correlation, "the greater the reduction of the fluctuating loads and dynamic response".

The spanwise correlation is calculated using the expression in Eq. (5):

$$R_{C_i}(\Delta z/D) = \frac{\mathrm{cov}\left(S_{z/D}, S_{(z+\Delta z)/D}\right)}{\sigma\left(S_{z/D}\right)\sigma\left(S_{(z+\Delta z)/D}\right)}, \tag{5}$$

where S is the time-history of the variable for which the correlation is being calculated, z is the coordinate

in the spanwise dimension where the time-history is obtained, *cov* refers to the covariance of two variables and σ represents its standard deviation.

2.3 Modal decomposition

According to Taira et al. [28], modal decomposition is a set of general mathematical techniques that allow to extract energetically and dynamically important features in fluid flows. Based on this analysis, spatial mode shapes and characteristic values are obtained, the latter ones representing either the energy content levels, or growth rates and frequencies. These modes can be obtained from the flow field data or from the governing equations, which are also referred as data-based techniques and operated-based techniques [28]. In this manuscript only data-based techniques are applied to the pressure fields over the surface of the studied bluff bodies. In the following, the range of different modal decomposition techniques used in this work are reviewed.

2.3.1 Data matrix construction

Consider the n-dimensional vector field, at a given time, defined in Eq. (6):

$$\boldsymbol{q}_{ijk} = \left(u^1_{ijk}, \ldots, u^n_{ijk}\right) = \left(u^1\left(\xi_i, \eta_j, \mu_k\right), \ldots, u^n\left(\xi_i, \eta_j, \mu_k\right)\right), \tag{6}$$

whereξ_i, η_j and μ_k are the spatial coordinates, with$i = 1, \ldots, n_\xi$, j $= 1, \ldots, n_\eta$ and $k = 1, \ldots, n_\mu$, the number of point coordinates in each direction. The data row vector is formed by stacking each component of the data as illustrated in Eq. (7):

$$\begin{aligned}\boldsymbol{x}^T = \Big[&u^1_{111}, \ldots, u^1_{ijk}, \ldots, u^1_{n_\xi n_\eta n_\mu}, u^2_{111}, \ldots, u^2_{ijk}, \ldots, \\ &u^2_{n_\xi n_\eta n_\mu}, \ldots, u^n_{111}, \ldots, u^n_{ijk}, \ldots, u^n_{n_\xi n_\eta n_\mu}\Big],\end{aligned} \tag{7}$$

hence the column vector is $\boldsymbol{x} = \left(\boldsymbol{x}^T\right)^T$. This column vector is generated for every temporal snapshot in the simulations or experiment. Therefore the final data matrix is:

$$\boldsymbol{X} = \left[\boldsymbol{x}\left(t_1\right), \boldsymbol{x}\left(t_2\right), \ldots, \boldsymbol{x}\left(t_n\right)\right]. \tag{8}$$

2.3.2 Proper orthogonal decomposition

The proper orthogonal decomposition (POD) provides a way to express the random field in a series of mutually uncorrelated structures that are optimal for expressing the total variance [26]. This technique enables for example the identification of coherent structures from turbulent flow-fields by extracting modes based on the "*optimisation of the mean square of the field variable under study*" [28]. In the present study, the time-dependent pressure distribution on the bluff body surface is adopted as the field variable of interest, so that the pressure distribution might be reconstructed from the minimal number of modes, containing as much energy as possible.

The algorithm for calculating POD modes starts by subtracting from a vector field $\boldsymbol{q}(\xi, t)$ its mean field $\overline{\boldsymbol{q}}(\xi)$ and assuming that the fluctuating component of the vector field can be decomposed as follows:

$$\boldsymbol{x}(t) = \boldsymbol{q}(\xi, t) - \overline{\boldsymbol{q}}(\xi) = \sum_j a_j(t)\boldsymbol{\phi}_j(\boldsymbol{\xi}), \tag{9}$$

where $\phi_j(\xi)$ are the spatial modes and $a_j(t)$ are the expansion coefficients.

The spatial data are allocated in a column vector $\boldsymbol{x}\left(t_i\right)$ for every temporal snapshot, stacked as described in Sect. 2.2.1, yielding matrix $\boldsymbol{X}$.

$$\boldsymbol{X} = \left[\boldsymbol{x}\left(t_1\right), \boldsymbol{x}\left(t_2\right), \ldots, \boldsymbol{x}\left(t_m\right)\right] \in \mathbb{R}^{n \times m}, \tag{10}$$

where n is the number of spatial locations and m is the number of time steps.

The covariance matrix $\boldsymbol{R}$ is calculated from the data matrix as shown in Eq. (11):

$$\boldsymbol{R} = \sum_{i=1}^{m} \frac{\boldsymbol{x}\left(t_i\right)\boldsymbol{x}^T\left(t_i\right)}{m-1} = \frac{\boldsymbol{X}\boldsymbol{X}^T}{m-1} \in \mathbb{R}^{n \times n}. \tag{11}$$

The modes $\boldsymbol{\phi}_i$ are calculated by solving the eigenvalue problem in Eq. (12), which are the eigenvectors of the problem, and they are orthonormal among them.

$$\boldsymbol{R}\boldsymbol{\phi}_j = \lambda_j \boldsymbol{\phi}_j, \phi_j \in \mathbb{R}^n, \lambda_1 \geq \cdots \geq \lambda_n \geq 0. \tag{12}$$

The eigenvalues λ_j represent the energy content of each mode, allowing its sorting as well as providing an indication about how many modes are needed

in order to properly represent the fluctuations in the flow-field data.

$$\frac{\sum_{j=1}^{r}\lambda_j}{\sum_{j=1}^{n}\lambda_j} \approx 1, \tag{13}$$

where r is the number of modes considered for the reconstruction of the field.

Finally, the temporal coefficients are calculated as indicated in Eq. (14):

$$a_j(t) = \langle \boldsymbol{q}(\xi,t) - \overline{\boldsymbol{q}}(\xi), \boldsymbol{\phi}_j(\xi)\rangle = \langle \boldsymbol{x}(t), \boldsymbol{\phi}_j\rangle, \tag{14}$$

where $\langle\rangle$ represents the inner product.

If the number of temporal snapshots is smaller than the number of locations ($m < n$), it is possible to calculate the POD modes using the *method of snapshots*. In the later approach, the solved eigenvalue problem is:

$$\boldsymbol{X}^T\boldsymbol{X}\boldsymbol{\psi}_j = \lambda_j\boldsymbol{\psi}_j, \boldsymbol{\psi}_j \in \mathbb{R}^m. \tag{15}$$

Then, the original POD modes can be calculated as:

$$\boldsymbol{\phi}_j = \boldsymbol{X}\boldsymbol{\psi}_j\frac{1}{\sqrt{\lambda_j}} \in \mathbb{R}^n, \quad j = 1,2,\ldots,m. \tag{16}$$

According to Taira et al. [28], travelling structures of real-valued POD modes cannot be represented by a single mode. Instead, they are represented by a pair of stationary POD modes, similar among them, and shifted in the advection direction.

2.3.3 Spectral POD

Spectral POD (SPOD) is a modal decomposition technique which provides time-harmonic modes at discrete frequencies from a set of realisations of the temporal Fourier transform of the flow-field [28]. As opposed to the POD modes, whose spectrum contains multiple frequencies, the spectrum of each SPOD mode contains a single frequency.

In order to calculate the SPOD modes, first the time series of the considered snapshots for the flow variable of interest is divided in a number n_b of overlapping blocks. Then, the temporal Fourier transform for each block is calculated. In Eq. (17), this transformation is presented for block l:

$$\widehat{\boldsymbol{X}}^{(l)} = \left[\widehat{\boldsymbol{\omega}}_1^{(l)}, \widehat{\boldsymbol{\omega}}_2^{(l)}, \widehat{\boldsymbol{\omega}}_{m_{FFT}}^{(l)}\right] \in \mathbb{R}^{n\times m_{FFT}}, \tag{17}$$

where n is the number of points times the number of components of the field under study, one for a pressure field and three for a flow velocity field for instance, meanwhile m states the number of frequencies in which the temporal time-history was decomposed after the Fourier analysis.

Afterwards, all the realisations of the Fourier transform at a specific frequency ω_k are collected into matrix $\widehat{\boldsymbol{X}}_{\omega_k}$:

$$\widehat{\boldsymbol{X}}_{\omega_k} = \left[\widehat{\boldsymbol{x}}(\omega_k)^{(1)}, \widehat{\boldsymbol{x}}(\omega_k)^{(2)}, \widehat{\boldsymbol{x}}(\omega_k)^{(n_b)}\right]. \tag{18}$$

Finally, the covariance matrix is calculated, and the eigenvalue problem is solved for each frequency, yielding the SPOD modes $\boldsymbol{\phi}'_{w_{k,j}}$ and their corresponding modal energies $\lambda_{\omega_{k,j}}$:

$$\widehat{\boldsymbol{X}}_{\omega_k}\frac{\widehat{\boldsymbol{X}}_{\omega_k}\widehat{\boldsymbol{X}}_{\omega_k}^T}{m_{FFT}-1}\boldsymbol{\phi}'_{\omega_{k,j}}, \boldsymbol{\phi}'_{\omega_{k,j}} \in \mathbb{R}^{n_b}, \lambda_{w_{k,1}} \geq \cdots \geq \lambda_{w_{k,n_b}} \geq 0. \tag{19}$$

For further information on the method, the interested reader can refer to the works of Taira et al. [28] and Schmidt et al. [26].

2.3.4 Dynamic mode decomposition

Following Taira et al. [28], the dynamic mode decomposition (DMD) is introduced as a technique which enables the decomposition of time-resolved data into modes. These modes are characterised by having a single frequency and growth/decay rate. DMD combines the best features of POD and the Fourier transform, providing a way to bring physical insights into a system.

The algorithm for the DMD calculation, according to Tu et al. [29], starts by rearranging the data in two matrices as follows:

$$\boldsymbol{X} = \left[\boldsymbol{x}(t_1), \boldsymbol{x}(t_2), \ldots, \boldsymbol{x}(t_m)\right] \in \mathbb{R}^{n\times m} \text{ and}$$
$$\boldsymbol{Y} = \left[\boldsymbol{x}(t_2), \boldsymbol{x}(t_3), \ldots, \boldsymbol{x}(t_{m+1})\right] \in \mathbb{R}^{n\times m}. \tag{20}$$

The relationship between these two matrices is linearly approximated as:

$$\boldsymbol{Y} = \boldsymbol{A}\boldsymbol{X}. \tag{21}$$

In order to calculate matrix $\boldsymbol{A}$ it is needed to calculate the standard value decomposition (SVD) of matrix $\boldsymbol{X}$.

$$\boldsymbol{X} = \boldsymbol{U}\boldsymbol{\Sigma}\boldsymbol{V}^T. \tag{22}$$

In the above equation $\boldsymbol{\Sigma}$ is a diagonal matrix with values$\sigma_1 \geq \sigma_2 \geq \cdots \geq \sigma_p \geq 0$. It is possible to truncate the SVD using the first r columns of $\boldsymbol{U}$ and $\boldsymbol{V}$, and the first r rows and columns of$\boldsymbol{\Sigma}$. Hence the truncated matrices $\boldsymbol{U}_r$, $\boldsymbol{V}_r$ and $\boldsymbol{\Sigma}_r$ are obtained by selecting the r rows and columns as stated.

Using the truncated matrices instead of calculating matrix $\boldsymbol{A}$, matrix $\widetilde{\boldsymbol{A}}$ is obtained:

$$\widetilde{\boldsymbol{A}} = \boldsymbol{U}_r^T\boldsymbol{A}\boldsymbol{U}_r = \boldsymbol{U}_r^T\boldsymbol{X}\boldsymbol{V}_r\boldsymbol{\Sigma}_r^{-1} \in \mathbb{R}^{r\times r}. \tag{23}$$

Then, it is needed to solve the following eigenvalue problem:

$$\widetilde{\boldsymbol{A}}\widetilde{\boldsymbol{\varphi}}_j = \mu_j\widetilde{\boldsymbol{\varphi}}_j, \tag{24}$$

with eigenvalues μ_j and eigenvectors $\widetilde{\boldsymbol{\varphi}}_j$. All the nonzero μ_j are DMD eigenvalues.

Finally, the DMD modes are calculated as:

$$\boldsymbol{\varphi}_j = \frac{1}{\mu_j}\boldsymbol{Y}\boldsymbol{V}_r\boldsymbol{\Sigma}_r^{-1}\widetilde{\boldsymbol{\varphi}}_j. \tag{25}$$

The growth/decay ratios of the DMD modes can be calculated from the real and imaginary components of λ_j, which are evaluated as:

$$\lambda_j = \frac{1}{\Delta t}log\left(\mu_j\right), \Delta t = t_{j+1} - t_j. \tag{26}$$

For further information about DMD decomposition, the interested reader is referred to Taira et al. [28] and Tu et al. [29].

3 Application case and computational model

The geometry under study in this piece of research is the one corresponding with the bare configuration of the Stonecutters bridge deck (see Fig. 1 for a graphical representation of its cross section) without considering the transversal beams connecting both boxes. The static simulation was conducted at a $\mathrm{Re}_D = UD/\upsilon = 4.48 \times 10^4$, the same as in Kwok et al. [16] adopting a 1/80 geometrical scale. In the case of the simulations undergoing heave oscillation, the swept range of Reynolds numbers was $\mathrm{Re}_D = 2.85 \times 10^3$ to $\mathrm{Re}_D = 3.81 \times 10^3$ as in Larsen et al. [17], with a $Sc = 32$ (A. Larsen, personal communication, July 3–4, 2018).

All the simulations reported here have adopted a 3D geometry, considering a Smagorinsky LES turbulence model [25], solved with the CFD software OpenFOAM 5.0 [12]. The diffusive terms were discretised by using the second order central difference scheme while the second order upwind differencing scheme has been applied for the convective terms. Advancement in time was performed by the second order backward scheme. Finally, the pressure–velocity coupling was solved by the PIMPLE algorithm. In the dynamic simulations, the Arbitrary Lagrangian Eulerian approach was applied to incorporate the movement of the mesh into the governing fluid equations. The deck was partially restrained, allowing displacements only in the heave degree of freedom, and its oscillation was modelled by a single-degree-of-freedom mass-spring-damper system. The coupling between the fluid, the structural system and the dynamic mesh was achieved by the use of the conventional serial staggered scheme.

The overall fluid domain is depicted in Fig. 2a, and its main dimensions are reported in Table 1. The spanwise length considered in this study is equal to the width of a single box, following the criteria used in authors' previous works [2, 3].

The boundary conditions imposed in the simulations were Dirichlet type conditions for the velocity and turbulent viscosity at the inlet, meanwhile Neumann conditions were imposed for the inlet pressure. At the outlet, Dirichlet conditions were applied to the pressure, and Neumann type conditions to the velocity and turbulent viscosity. For the upper, lower and lateral faces, symmetric boundary conditions were applied, as they provide physically sounder spanwise

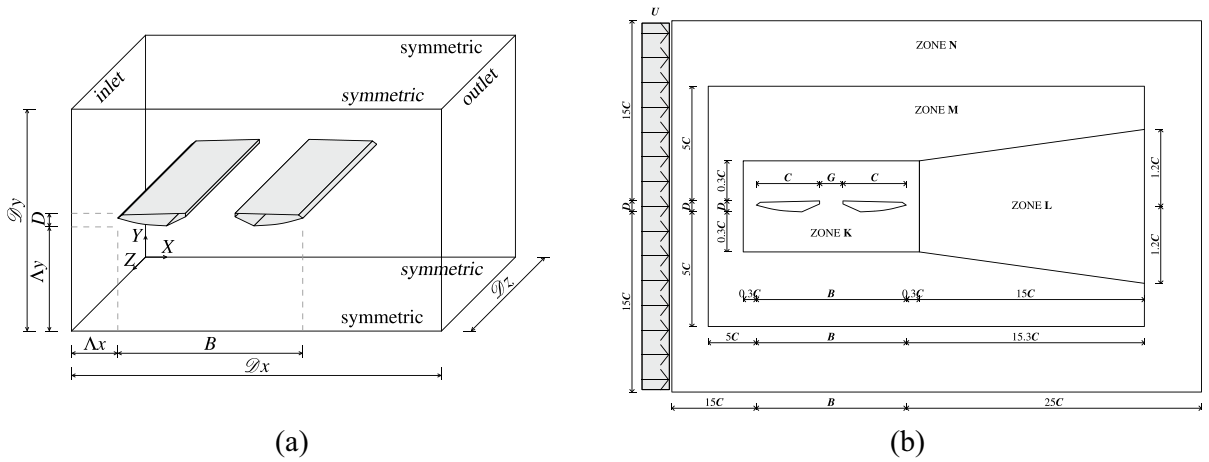

Fig. 2 **a** Overall fluid domain and **b** different zones in which the XY plane mesh is subdivided. (Not to scale)

Table 1 Overall fluid domain dimensions. B is the deck width, and C and D are the width and height of each individual box. (See Fig. 2 for the graphical definition of the flow domain variables.)

Λ_x	Λ_y	$\mathcal{D}_x$	$\mathcal{D}_y$	$\mathcal{D}_z$
$15C$	$15C$	$40C+B$	$30C+D$	C

correlations [3]. In all the simulations the turbulence intensity at the inlet is negligible, similar to the experimental tests. For the twin-box deck walls, no-slip and no-penetration boundary conditions were applied [30].

The mesh of choice used for the spatial discretisation of the fluid domain was a structured quadrangular mesh for the boundary layer region around the boxes and the spanwise dimension, meanwhile for the rest of the XY plane an unstructured quadrangular mesh was adopted. As in previous works by the authors [2], the XY plane has been subdivided in different regions aiming at efficiently handle the mesh density grading. The fundamental outline for the finite volume mesh is presented in Fig. 2b. Graphical details of the mesh in

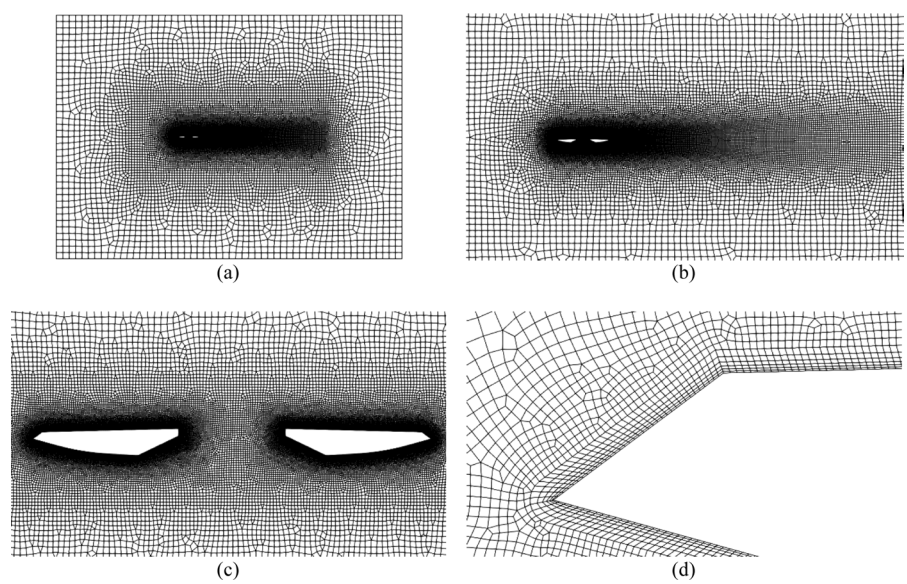

Fig. 3 Mesh discretisation details of the medium mesh. **a** overall fluid domain, **b** buffer zone and wake, **c** mesh around the deck and **c** boundary layer detail

the XY plane are shown in Fig. 3. The mesh was generated using the GMSH [11] open-source tool, yielding a mesh with 3,218,112 elements.

The mean y^+ values obtained for the static deck are always below 1.25, presenting a y^+ higher than 4 only in 4.5% of the elements, hence no wall functions are adopted to model the boundary layer behaviour. These y^+ values were obtained as indicated in Bruno et al. [6], although in this study it is considered the total height of the first element of the boundary layer for their calculation. Moreover, all the simulations have been conducted imposing a maximum Courant number of $Co = 1.0$, recording data every 4 time-steps. The time step is not constant, as it is controlled by the PIMPLE algorithm for enforcing $Co = 1.0$.

In the CFD simulations reported next, the mesh has been selected based on the verification study in Álvarez et al. [4], where the procedure proposed in Celik et al. [8] is applied. Validation of the CFD data with experimental tests in Kwok et al. [16] and Larsen et al. [17] was reported in Álvarez et al. [1]. In Table 2 the integral parameters for the static twin-box deck at 0º angle of attack are provided. In Fig. 4, the chart of heave amplitudes response vs. reduced velocity shows the ability of the 3D LES simulations to capture the VIV-prone region for the bridge. It is noticeable the accuracy in the identification of the peak heave oscillation at $U/(f_0 B) = 0.35$ (f_0 is the natural frequency of the one dimensional dynamic system and B the total width of the deck), which is adopted in Sects. 4 and 5 as application case for correlation and modal analysis.

The simulations were stopped when the convergence criterion defined in Bruno et al. [6], based on the limitation of changes in the variables of interest in successive time-windows, was met. This criterion was used for the integral parameters in the static simulations and for the amplitude of oscillation in the VIV simulations. The VIV peak amplitude simulation ($U/(f_0 B) = 0.35$) was extended for 2879.62 non-dimensional time units (tU/D), requiring 7.74 s/per core to calculate 1 non-dimensional time unit.

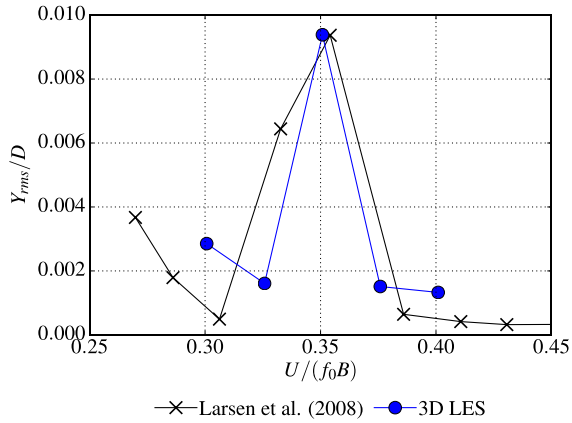

Fig. 4 Amplitudes of oscillation of the vertically free-to-oscillate simulations at different reduced velocities

In this piece of research, when referring to the analysis of the simulations undergoing VIV oscillations in heave, it is always considered the reduced velocity at the VIV peak amplitude response.

4 Spanwise correlations

4.1 Spanwise force coefficients correlation

The spanwise correlation of the time-dependent force coefficients provides information about the organisation of the vortical structures: the higher the correlation value the more organised these structures are. Hence, it is also giving information about the intensity of the fluctuating loads acting on the structure.

In Fig. 5, these correlations depending on the spanwise length are graphically presented for both the static and the vertically free-to-oscillate cases [1]. The static deck simulation was conducted at a $\mathrm{Re}_D = 4.48 \bullet 10^5$ meanwhile the VIV case corresponds with the peak oscillation amplitude at a reduced velocity $U/(f_0 B) = 0.35$, and $\mathrm{Re}_D = 3.33 \cdot 10^3$. The force coefficients have been calculated by integrating the pressures over 49 equi-spaced strips along the deck spanwise dimension.

Table 2 Integral parameters:

	$\overline{C_d}$	$\overline{C_l}$	$\overline{C_m}$	$\widetilde{C_d}$	$\widetilde{C_l}$	$\widetilde{C_m}$	St
Present study	0.153	− 0.260	0.206	0.027	0.202	0.090	0.244
Kwok et al. [16]	0.140	− 0.234	0.268	–	–	–	0.278

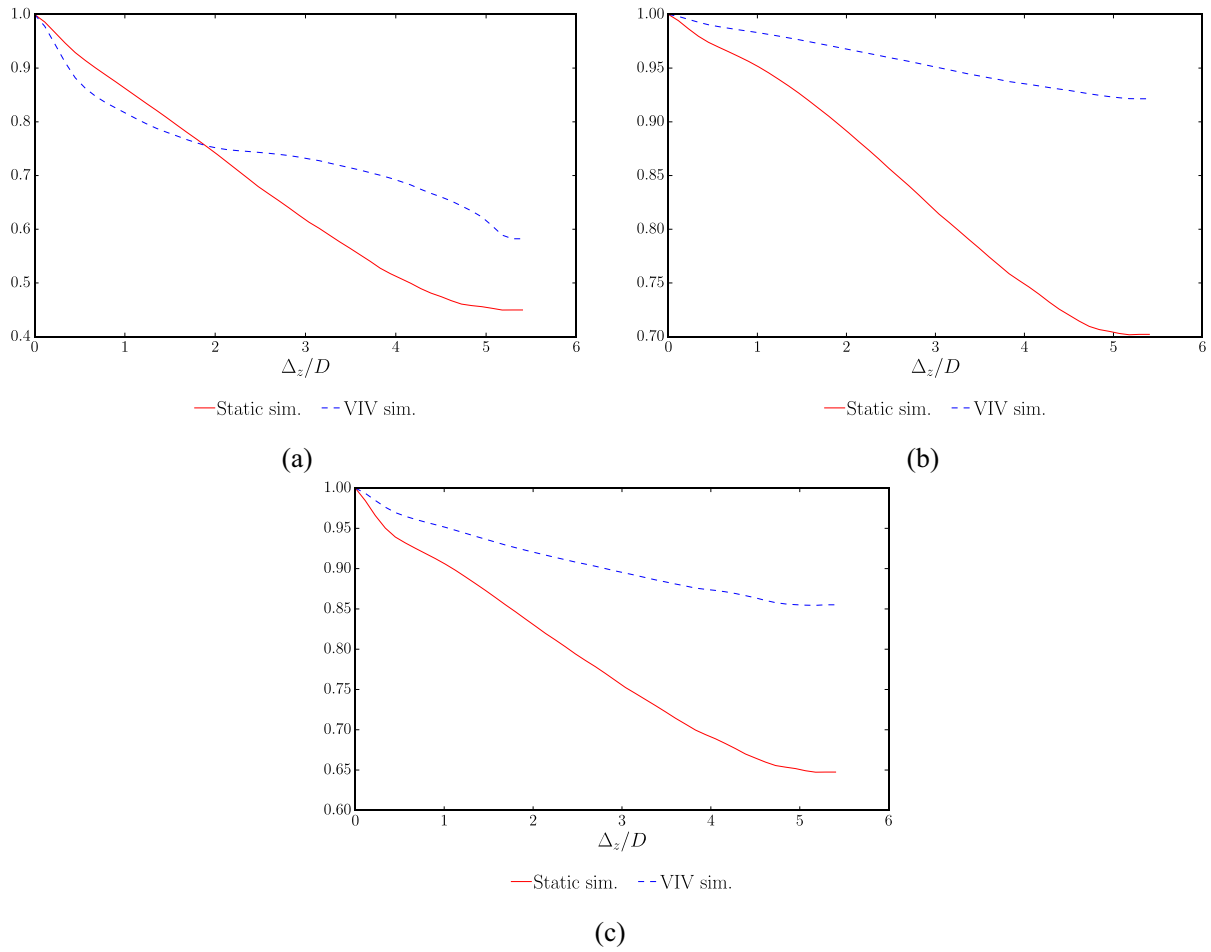

Fig. 5 Spanwise force coefficient correlations, **a** drag, **b** lift and **c** moment

In Fig. 5, it may be noticed how the vertically free-to-oscillate simulation presents higher correlation values than the static one. This effect can be explained by the reorganisation of the flow structures and vortex shedding fequency at lock-in due to periodic motion, generating more coherent spanwise structures, almost becoming perfectly correlated for the lift and moment coefficients. The increase in the correlation coefficients has been observed also in the experiments of a ratio 5:1 rectangular cylinder in Ricciardelli [21].

The phase-averaged correlation coefficient vs non-dimensional spanwise distance curves, for the force coefficients, are very similar among the different positions along the cycle of heave oscillation. For brevity sake, in Fig. 6 only the results for the lift coefficient are presented, as it is the most important forcing load during heave oscillations. The lower correlation value is attained at P1, at the oscillation peak (see Fig. 6c), meanwhile the maximum correlation value is obtained at P7, at midway in the increasing heave oscillation part of the signal, when the deck upward velocity is at its greatest value.

In Table 3, the integral of the area under the correlation coefficient curve for drag, lift and moment coefficients at different positions along the cycle of heave oscillation, relative to the perfect correlation case, are presented.

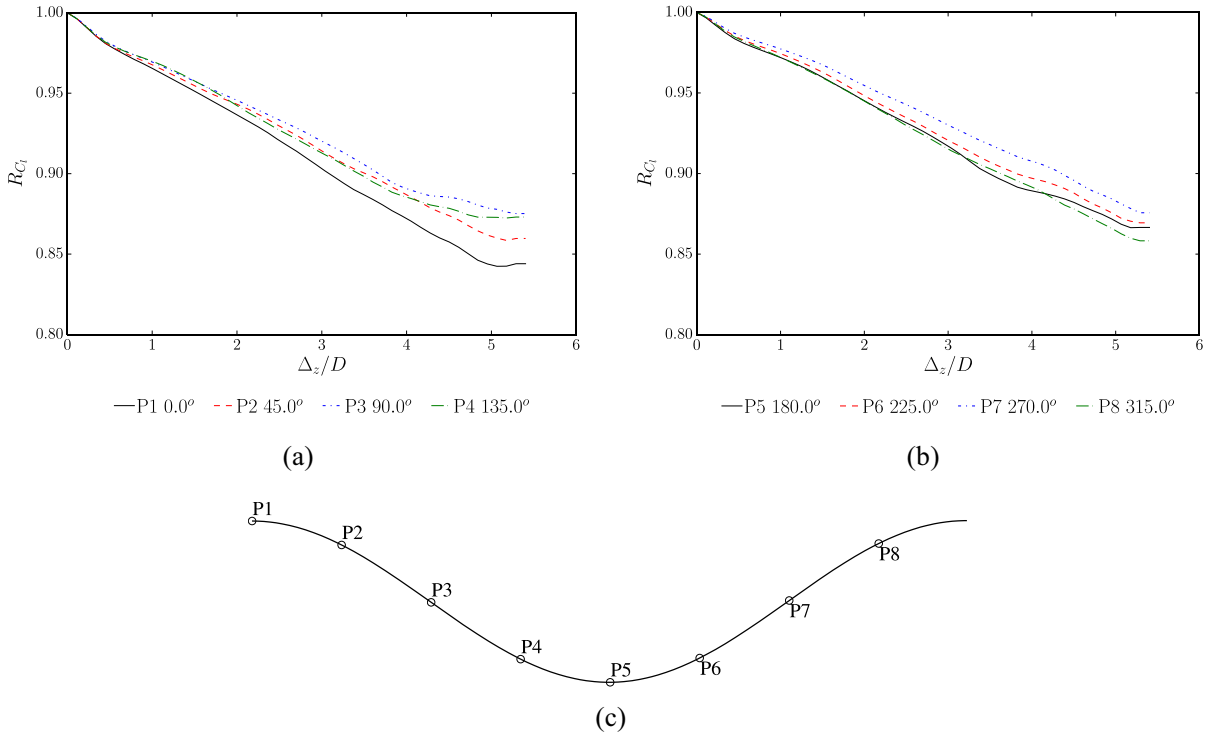

Fig. 6 Phase-averaged spanwise lift coefficient correlations over the cycle of heave oscillation, **a** lift P1 to P4, **b** lift P5 to P8 and **c** phase-averaged oscillation cycle

Table 3 Values of the integral over the spanwise length of the phase-averaged correlation coefficient distributions with respect perfect correlation, at eight positions over the cycle of heave oscillation.)

Position	P1	P2	P3	P4	P5	P6	P7	P8
$\int R_{C_d}(\Delta_z/D)d(\Delta_z/D)/\int 1d(\Delta_z/D)$	0.735	0.726	0.723	0.700	0.764	0.785	0.790	0.753
$\int R_{C_l}(\Delta_z/D)d(\Delta_z/D)/\int 1d(\Delta_z/D)$	0.914	0.923	0.928	0.924	0.927	0.931	0.937	0.926
$\int R_{C_m}(\Delta_z/D)d(\Delta_z/D)/\int 1d(\Delta_z/D)$	0.908	0.908	0.896	0.886	0.878	0.888	0.903	0.908

4.2 Spanwise pressure correlation

The spanwise correlations of the force coefficients provide limited information about the general organization of the flow, falling to address the complex three-dimensional features associated with flow separation, reattachment and the impinging vortices on the downstream deck. Conversely, the analysis of how the pressure coefficient correlations are distributed over the deck surfaces enables the deciphering of the complex flow structures interacting with the twin-boxes. First, in Fig. 7, the convention adopted to identify the upper and lower surfaces in the deck, the magnitude convention for the curvilinear coordinate S, and the corner naming are depicted. These are used hereunder to report and discuss the pressure correlations and pressure modes. Note that charts correspond to the flow moving from left to right at 0º angle of attack.

In order to record the pressures acting on the deck surfaces over time, two different approaches are available in OpenFOAM: (i) defining probes location coordinates and (ii) saving the data associated with the nodes of the corresponding wall patches. The approach based on probes generates a single very large file and needs to update the probe coordinates when the studied object is moving. This update needs

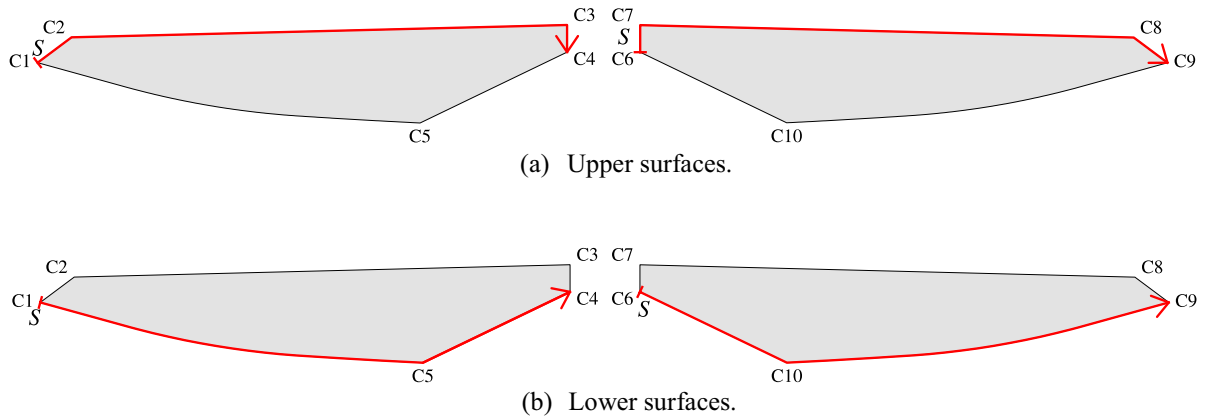

Fig. 7 Identification of the surfaces over which pressure correlation and pressure modes will be represented. (S is the curvilinear coordinate)

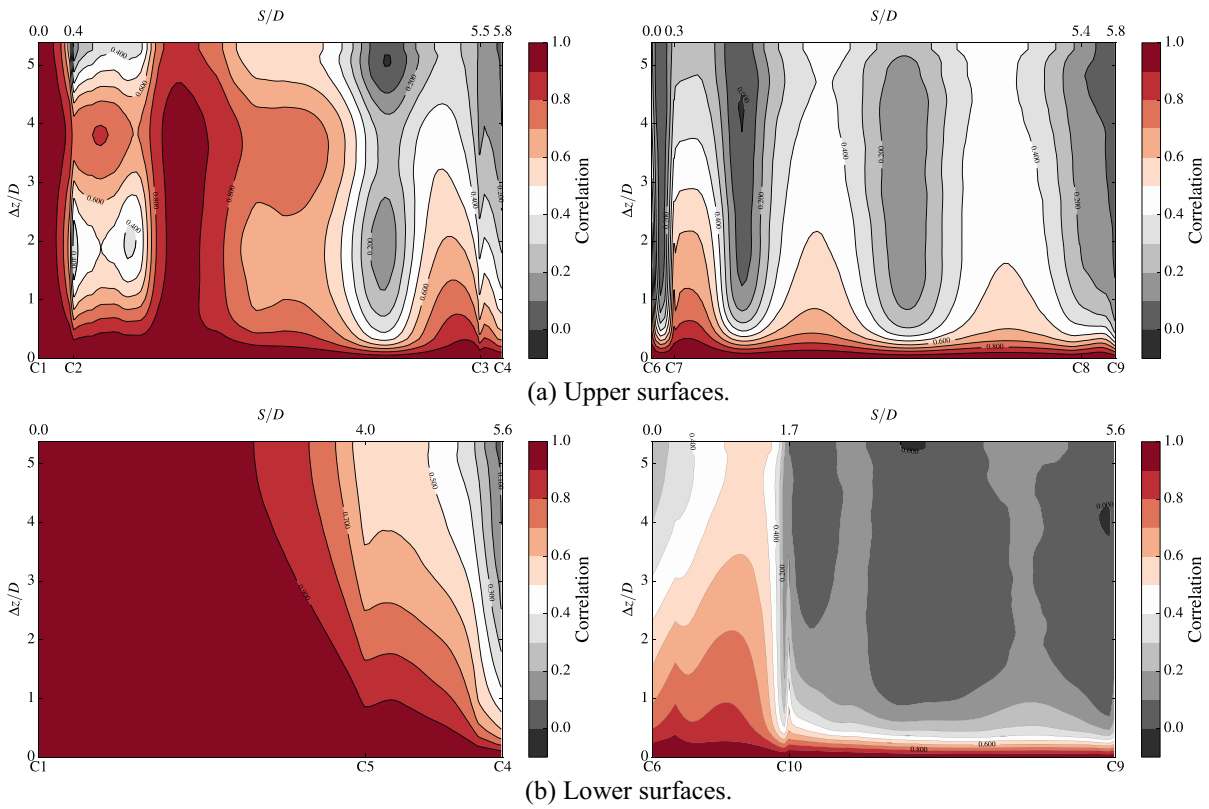

Fig. 8 Spanwise pressure correlation surface for the static deck case

to be done by means of an in-house script when the simulation has to be restarted. On the other hand, the approach based on the patches, needs no updating, but it generates a single file for every time-step stored. Therefore, in order to obtain the complete time-history, the data coming from multiple files has to be put together. HPC facilities usually have clock time constraints for single runs, along with limits in

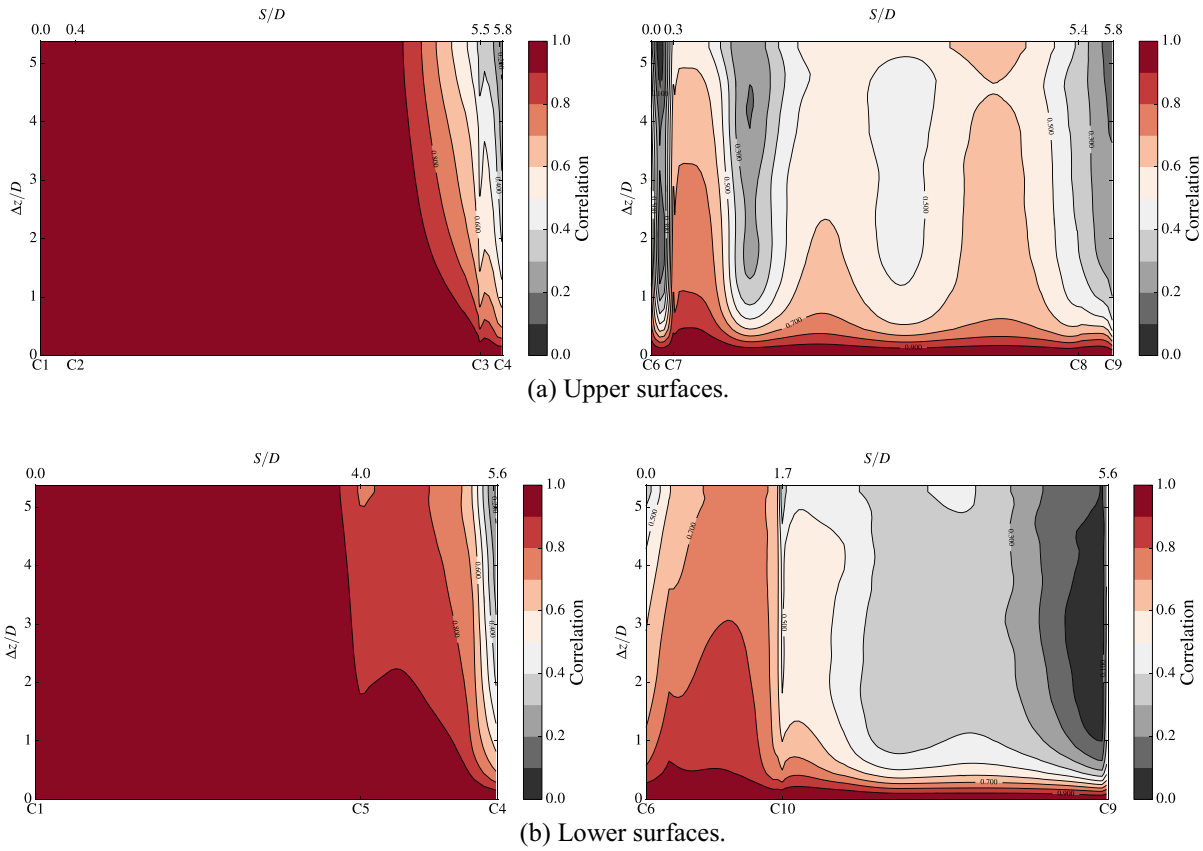

Fig. 9 Spanwise pressure correlation surface for the vertically free-to-oscillate simulation at $U/\left(f_0 B\right) = 0.35$

storage capacity and number of saved files. Awareness about these limitations is required in order to choose the right approach, considering that eventually the simulation should be restarted to obtain complete time-histories for the analysis of the addressed problem.

In Figs. 8 and 9, the spanwise pressure correlation coefficient distributions are presented for the same cases as in Sect. 3.1, that is the static deck and the heave VIV case at $U/\left(f_0 B\right) = 0.35$ (peak oscillation). It is to note that the values of the correlation coefficients are higher over all the deck surfaces when the deck is undergoing vortex induced vibration (VIV) oscillations at $U/\left(f_0 B\right) = 0.35$, in agreement with the higher correlation obtained for the force coefficients at VIV in Sect. 4.1 (Fig. 5). As reported in Álvarez et al. [2], the alternation of regions presenting high and low correlation coefficient values, are related with different flow regions based on the flow topology: separation, recirculation and reattachment.

Focusing on the static case (see Fig. 8a), on the windward box upper surfaces, the first half according to the curvilinear abscissa S, showing high pressure coefficient correlation values, is related with the recirculation region. Moving downwind, the flow reattaches and keeps attached along the remaining upwind box upper panel length, although with decreasing spatial coherence. The subsequent increment in the correlation coefficient values approaching the vicinity of the upwind box upper trailing edge can be explained due to the reorganisation in the flow

linked to the built up of vortices, previous to their shedding in the gap. On the other hand, a very different correlation distribution is appreciated over the upwind upper surfaces in Fig. 9a for the VIV peak oscillation case, where very high correlation coefficient values are found over the entire surface, meaning that single flow structures develop over the whole deck span due to the organizing effect of the lock-in.

Shifting the attention to the upper panels of the downwind box, a similar disposition of regions, alternating high and low correlation coefficient values, is presented in the two cases studied, although with higher values for the one undertaking VIV. This means that similar flow structures are developing in both cases, although with higher coherence and better organised structures in the spanwise dimension for the heave-excited deck at lock-in. The lower correlation coefficient values in the vertical panel facing the gap are due to the impingement of the highly three dimensional vortices shed from the upper trailing edge of the upwind box. Downwind from corner C7, after a strip of high correlation values linked to flow separation at C7 and the subsequent recirculation bubble, a low correlation coefficient value region is found, which is associated with the time-dependent flow reattachment position. Downwind this reattachment strip, the flow remains attached over the rest of the upper panel. The succession of high, low and high correlation coefficient values, downwind reattachment, may be interpreted respectively as the effect caused by:

- the drifting vortices shed from the separation bubble,
- their gradual dissipation,
- and the built up of vortices responsible for the weak vortex shedding in the wake of the downwind box.

Further discussions can be found in Álvarez et al. [2] for the static twin-box deck, noting that in the aforementioned reference a different geometric scale was adopted, along with a different spatial discretisation in the CFD model, as well as different time lengths for the calculation of the correlations.

For the static simulation, as the vortices shed from the downwind box are much weaker than the ones detaching from the upwind one, the general increment observed in the correlation coefficient values prior to reaching corner C8 is also smaller than in the vicinity of the upwind corner C3.

Focusing now on the analysis of the lower panels (Figs. 8b and 9b), it can be noted that both simulations present very similar pressure correlation coefficient distributions; although with slightly higher values for the VIV at lock-in case. The correlation coefficient starts to decrease near corner C5, and remarkably over the inclined panel facing the gap due to flow separation at C5. On the other hand, on the windward inclined panel of the downwind box, the correlation coefficient values increase from corner C6 towards corner C10, reaching a maximum near C10. The reduced values in the correlation coefficients in the vicinity of C6 are due to the impingement of the three-dimensional vortices shed from the upwind box, which then roll over the panel as the flow progresses downwind, building up near C10 before being shed again at that same corner. Finally, over the lower curved panel of the downwind box, a flow separation bubble forms, extending downwind and reaching the region of low correlation values. In this zone, the flow is recirculating, and between this point and the next correlation relative maximum, reattached flow is taking place. Downwind, the flow separates from the leeward box.

4.3 Phase averaged pressure correlation

As for the force coefficients, the phase averaged pressure correlation coefficients have been calculated for the same 8 instants along one period of oscillation, observing how they evolve through-out this cycle. In Figs. 10 and 11, the pressure correlation coefficient distributions for points P1 and P7, where the lift coefficient presents its minimum and maximum correlation respectively, are shown. It can be seen in the figures that the distributions corresponding with

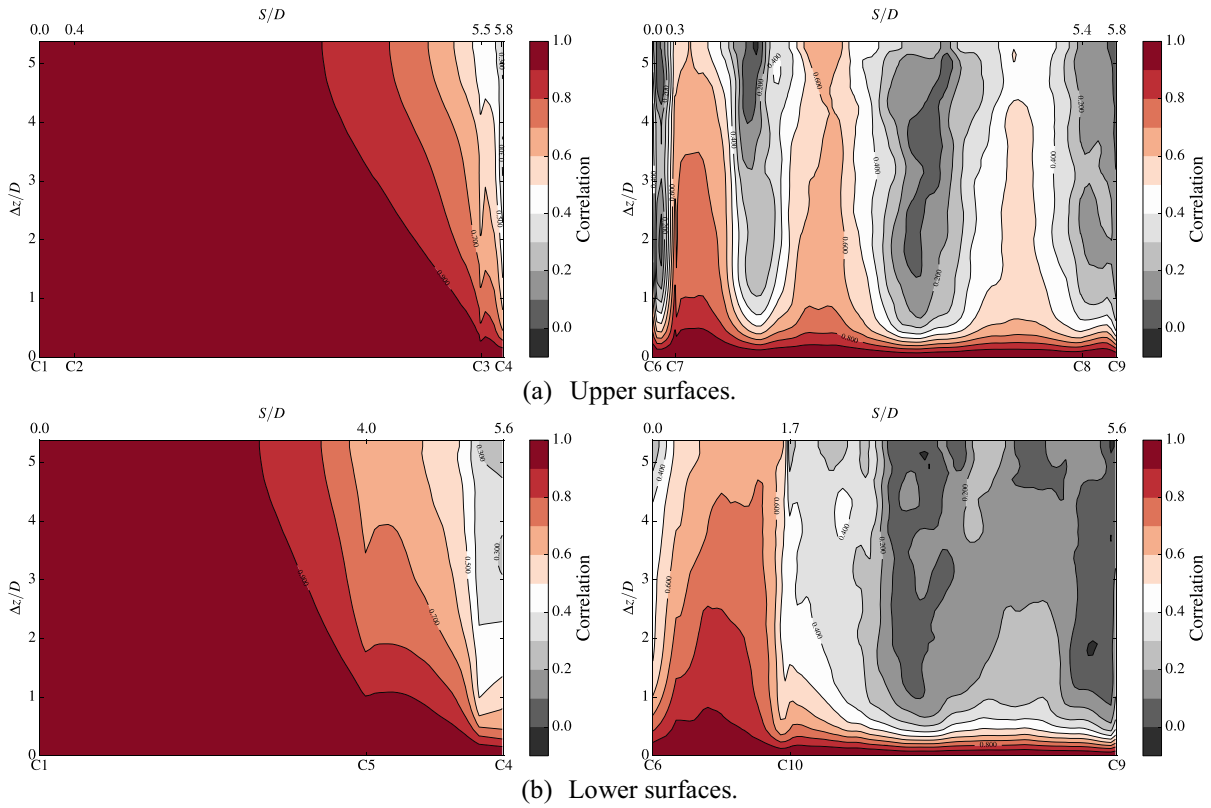

Fig. 10 Phase averaged spanwise pressure correlation surface for the vertically free-to-oscillate simulation at P1

P1 present lower values in the correlation coefficient than the ones in P7. The main difference between P1 and P7 is that in P7 the upwind box shows a larger surface with correlation values in the range (0.9, 1.0), in both the upper and lower surfaces. This helps to understand the important role played by the upwind box in the VIV response at the oscillation peak, as the differences in the phase-averaged correlation values over the down-wind box do not show distinctive features over the oscillation cycle.

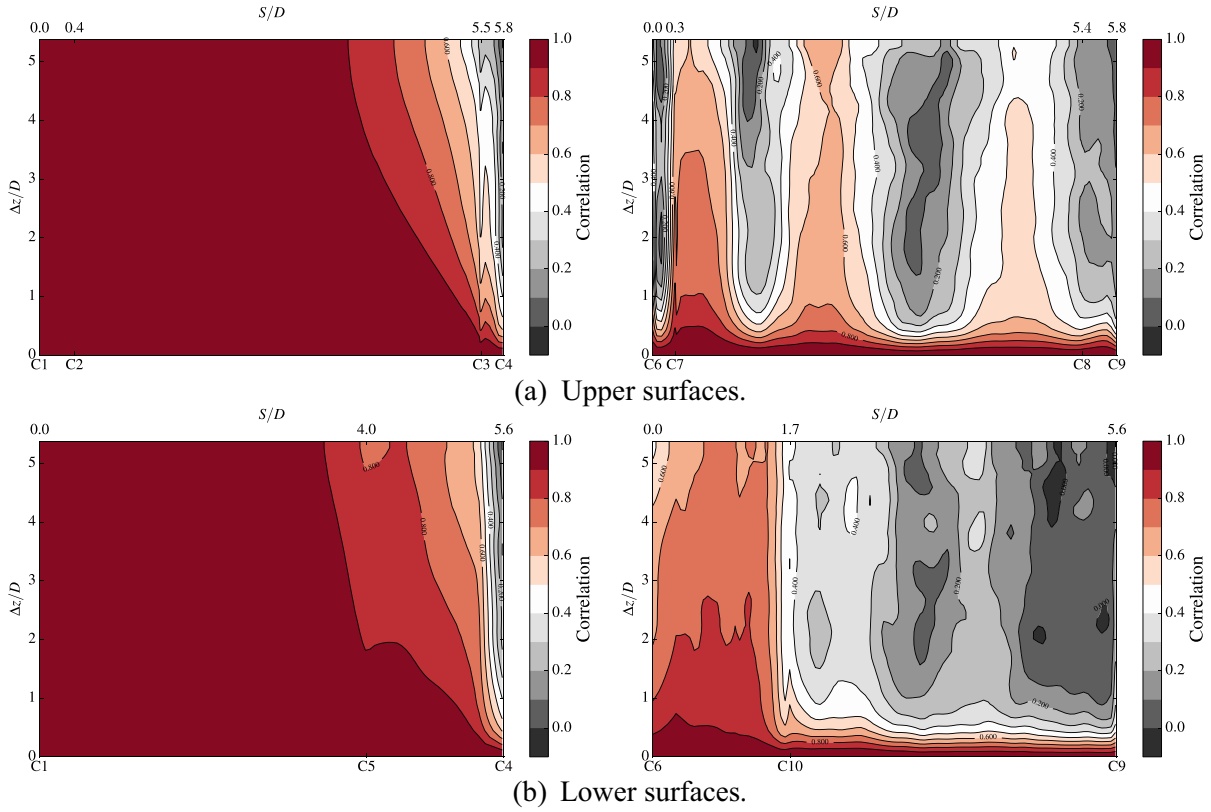

Fig. 11 Phase averaged spanwise pressure correlation surface for the vertically free-to-oscillate simulation at P7

5 Modal decomposition of the time-dependent pressure distributions

In this section, three different modal decomposition techniques, previously introduced in Sect. 2, are applied to shed additional light on the main features of the fluctuating pressure field over the surfaces of the deck. These decomposition methods provide tools for identifying the pressure footprints caused by the main flow structures, and each one addresses the limitations of the others, so they provide a more complete vision of the aerodynamic or aeroelastic phenomena taking place. Furthermore, the modal decomposition of the pressure distributions is instrumental for the subsequent application in Reduced Order Models (ROM) for VIV risk assessment [20, 22].

5.1 POD modal analysis

5.1.1 POD eigenvalues

POD analysis of the time-dependent pressure distributions around the deck permits the identification of coherent structures [13], based on the regularity of mode shapes. In the studied case, the contribution of each mode to the total energy is presented in Fig. 12, for both the static and the VIV cases at peak oscillation for comparison. It can be appreciated how the first mode of the peak VIV simulation contains more than half of the total energy of the process, which is nearly a 10% higher than the contribution of the first mode in the static case. In general, for both the static and peak VIV cases, the successive modes show a similar individual energy contribution in the process, as it may be perused in Fig. 12b.

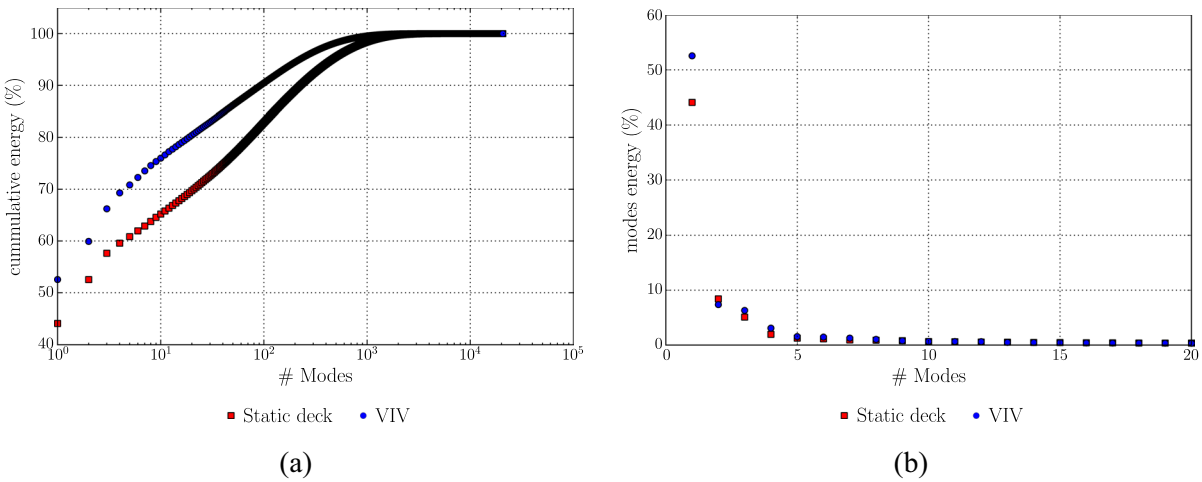

Fig. 12 Energy contribution of each mode, **a** cumulative and **b** individual

5.1.2 POD modes for the static twin-box deck

In Figs. 13 and 14, the graphical representation of the first three POD modes of the pressure distribution around the static deck are presented for each box. The first mode (Fig. 13) contains the 44.12% of the total energy, meanwhile the second and third modes (Fig. 14) contain the 8.41% and 5.09%. According to Oberleithner et al. [19], coupled modes typically show a similar amount of energy and pair in the POD spectrum; moreover, according to Taira et al. [28], real-valued POD modes cannot represent travelling flow structures as a single mode, so they are usually represented by a pair of stationary POD modes, which are similar, but appear shifted in the advection direction, that is they are almost symmetrical with respect to the flow direction. For these reasons, the second and third modes are presented in Fig. 14, as they are

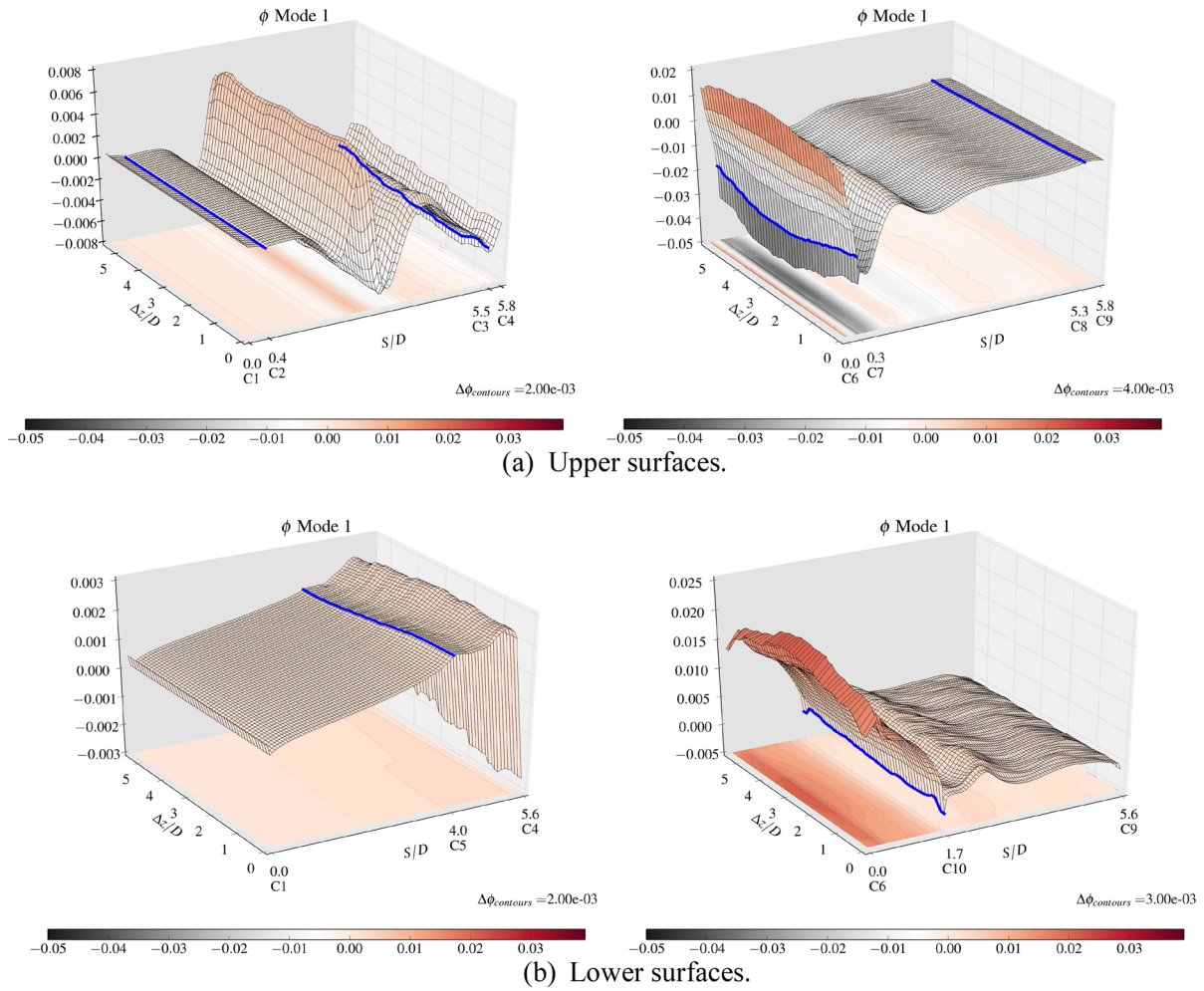

Fig. 13 First POD mode of the static simulation. (The blue lines represent the position of the deck corners)

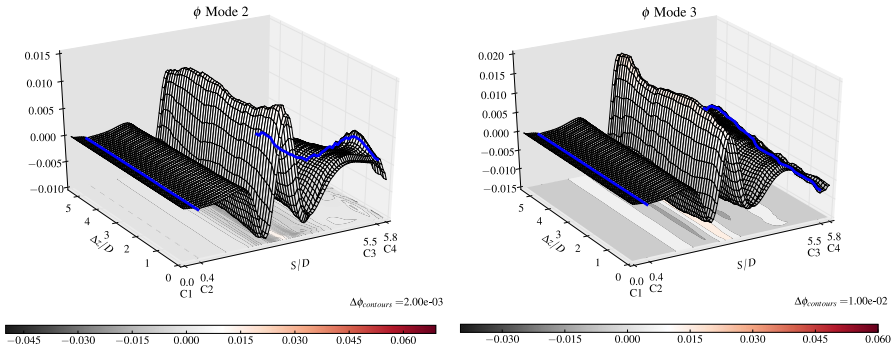

(a) Upper surfaces of the upwind box.

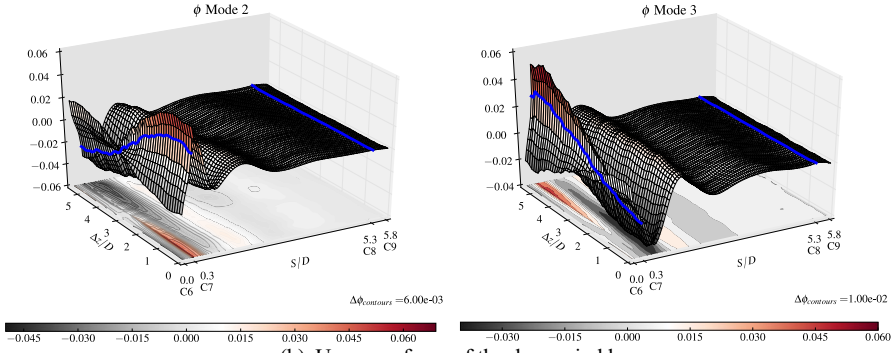

(b) Upper surfaces of the downwind box.

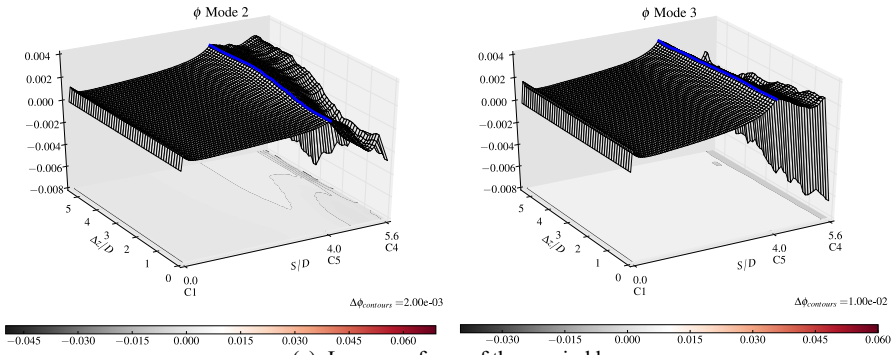

(c) Lower surfaces of the upwind box.

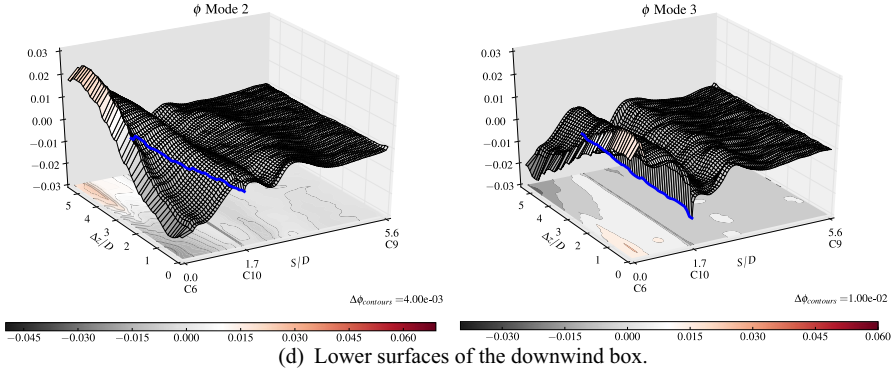

(d) Lower surfaces of the downwind box.

Fig. 14 POD modes of the static simulation corresponding with the second POD mode (left column), and with the third POD mode (right column). (The blue lines represent the position of the deck corners)

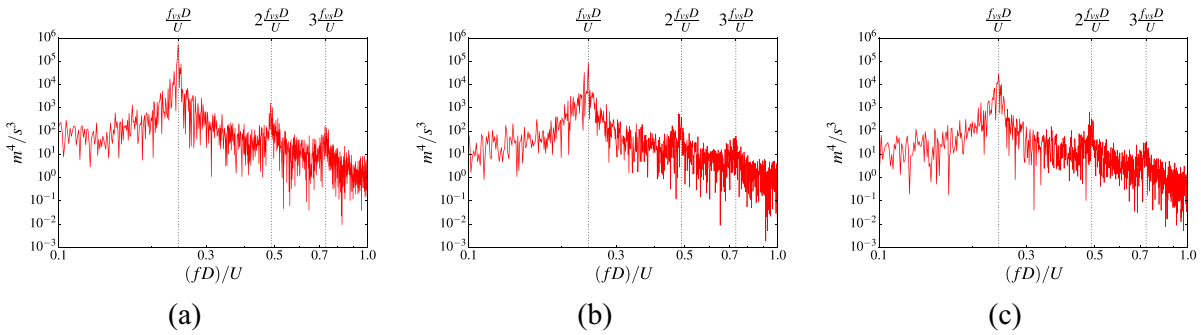

Fig. 15 Energy spectra from the POD modes of the static simulations: **a** first mode, **b** second mode and **c** third mode. (f_{vs} is the vortex shedding frequency. D is the height of the deck and U is the wind speed)

coupled, and represent the effects of the fundamental travelling flow structure associated with vortex shedding in the pressures over the deck. It is to note that the amplitude of modes 1, 2 and 3 at the downwind box are roughly one order of magnitude higher than for the upwind box, showing that the most important processes related with the pressure field over the deck are taking place on the downwind box.

In Fig. 15, the spectra of the first three POD modes are reported, containing a broad range of frequencies. Although the three modes show a main peak at the frequency corresponding with vortex shedding, two superharmonic frequency peaks can be identified. As expected, the spectra of the second and third modes are very similar among them, corresponding to coupled modes. It can be noticed that, as the energy content of the mode decreases, the magnitude of the peak frequencies in the spectra also decrease. These decrements in the energy values are due to less coherent structures that are present in lower energy modes.

5.1.3 POD modes at VIV peak response

The POD analysis has also been applied to the time-dependent deck pressure fields for the free heave oscillation case at $U/(f_0 B) = 0.35$. The first three mode shapes are depicted in Figs. 16 and 17. The first mode contains the 55.55% of the total energy in the pressure field, meanwhile the second and third modes present 7.37% and 6.29% respectively. Since the flow is better organised at lock-in, the amount of energy contained in the first mode is larger than in the static case. The geometry of the mode shape of the first VIV mode resembles the one of the static case, although the upper surface of the upwind box presents a smaller amplitude. On the other hand, the second and third modes present a higher coherence in the spanwise direction when compared with their static counterparts. As for the static simulations, the second and third mode of the VIV simulations are coupled, and represent the effect of travelling flow structure on the pressure distributions over the deck. Similarly to the static deck case, the amplitude of modes 1, 2 and 3 for the downwind box are significantly higher than for the upwind box.

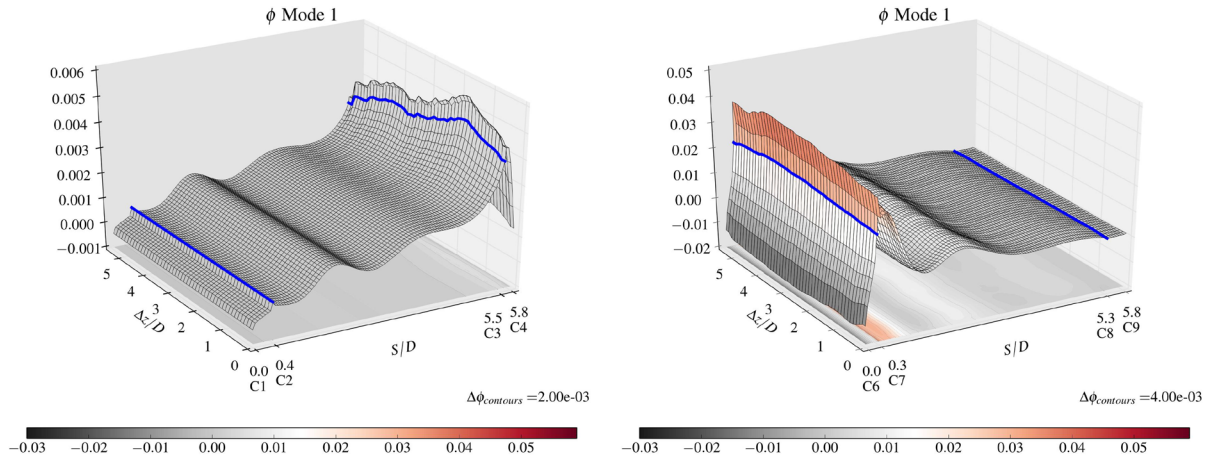

(a) Upper surfaces.

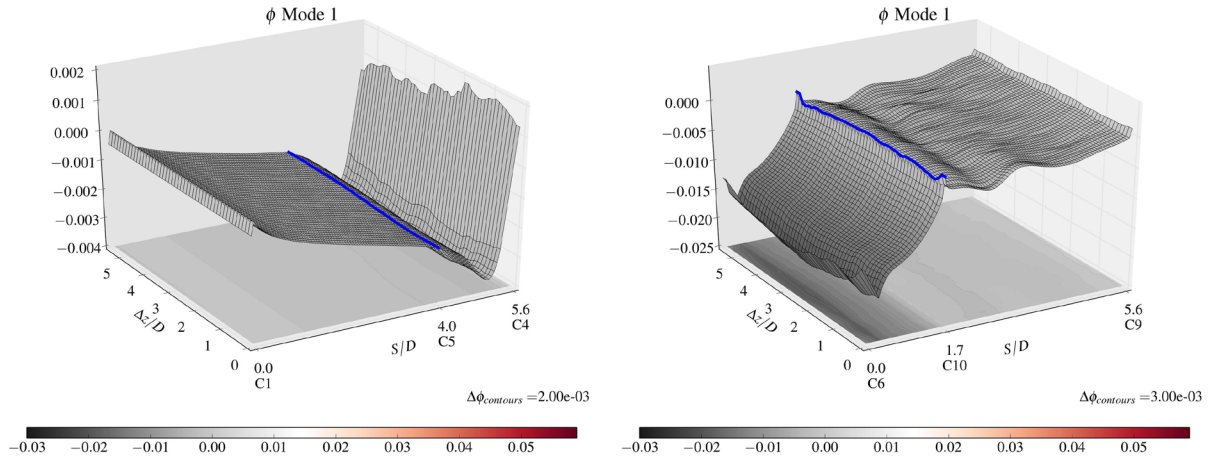

(b) Lower surfaces.

Fig. 16 First POD mode of the VIV simulation. (The blue lines represent the position of the deck corners)

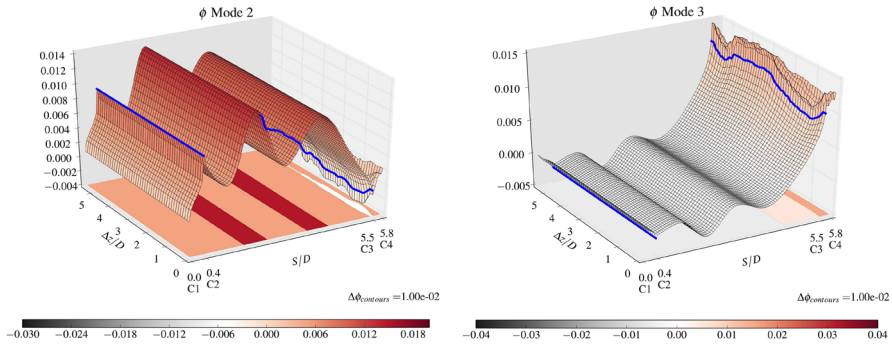

(a) Upper surfaces of the upwind box.

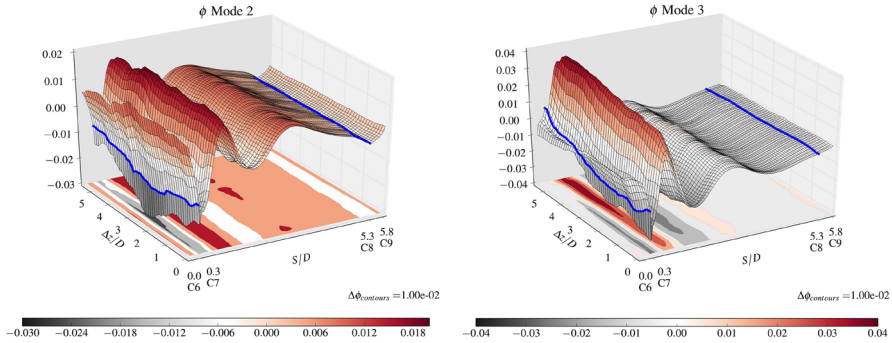

(b) Upper surfaces of the downwind box.

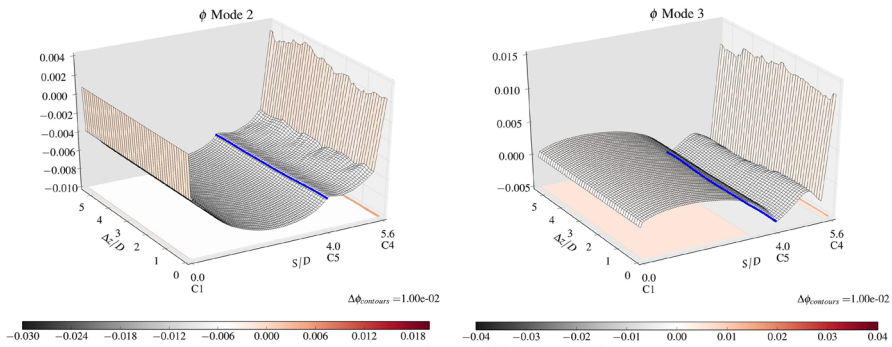

(c) Lower surfaces of the upwind box.

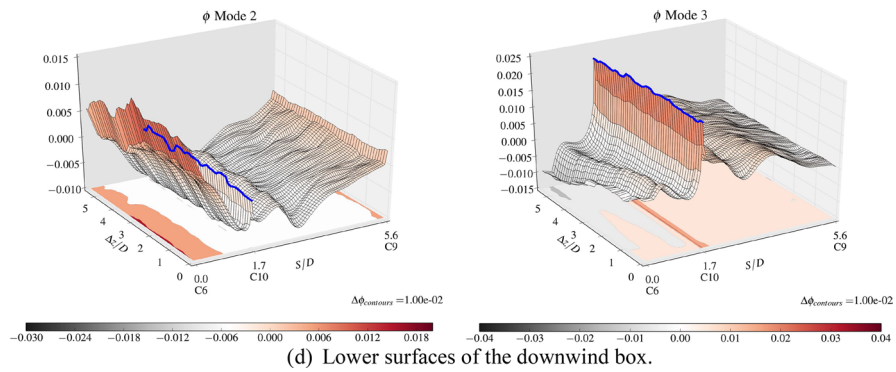

(d) Lower surfaces of the downwind box.

Fig. 17 POD modes of the VIV simulations corresponding with the second POD mode (left column), and with the third POD mode (right column). (The blue lines represent the position of the deck corners)

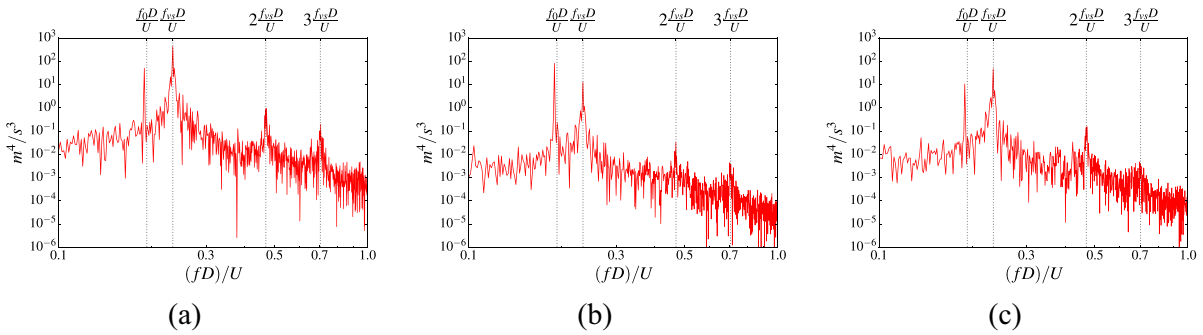

Fig. 18 Energy spectra from the POD modes of the VIV simulations: **a** first mode, **b** second mode and **c** third mode. (f_0 is the natural frequency of the heave system, f_{vs} is the vortex shedding frequency. D is the height of the deck and U is the wind speed)

In Fig. 18, the spectra of the first three modes of the pressure coefficient distribution undergoing VIV at the lock-in response are presented. It is interesting to note that the main frequency for mode one is the one corresponding with vortex shedding; meanwhile for modes 2 and 3, the frequency peak corresponds with the natural frequency of the dynamic system. These results are in full agreement with the study of the spectra of the heave oscillation and lift coefficient in the Álvarez et al. [1]. Similarly to the spectra obtained for the static deck case, two additional peaks associated with super-harmonics of the vortex shedding frequency can be identified.

5.2 SPOD modal analysis

Differently form the POD approach that provides modes containing multiple frequency contributions, the SPOD analysis provides modes associated with a single frequency content [26]. Although their identification requires a higher computational burden with respect the POD analysis, they provide data for the whole spectra of the field under study.

In Fig. 19, the spectra of the pressure field for the static and VIV simulations are presented. The total spectra is the red line, which for each frequency is the

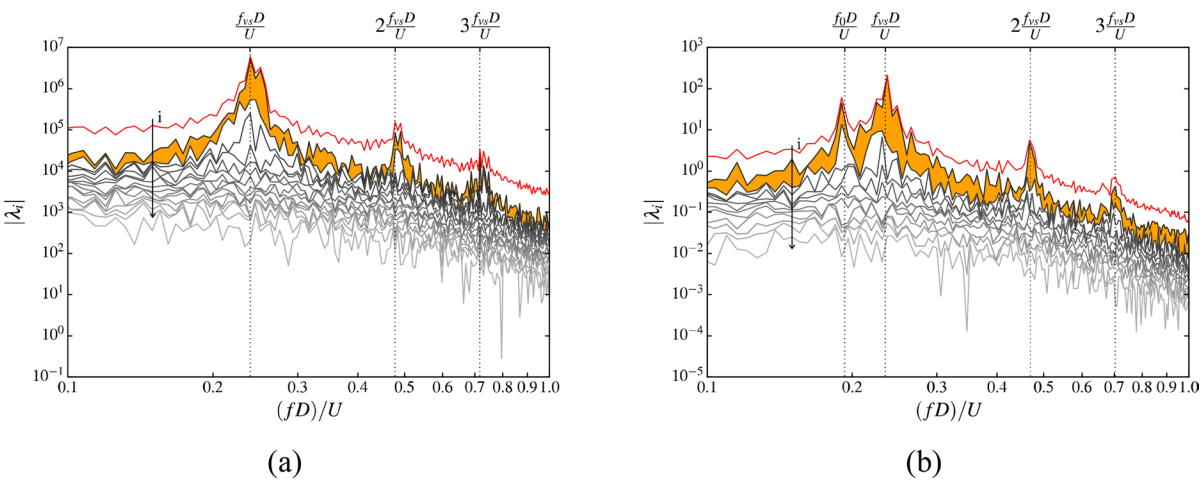

Fig. 19 Energy spectra from the SPOD modes (**a**) static simulation and (**b**) VIV simulation. (λ_i is the eigenvalue of the i mode for each frequency. i increases in the direction of the arrow) (f_0 is the natural frequency of the heave system, f_{vs} is the vortex shedding frequency. D is the height of the deck and U is the wind speed)

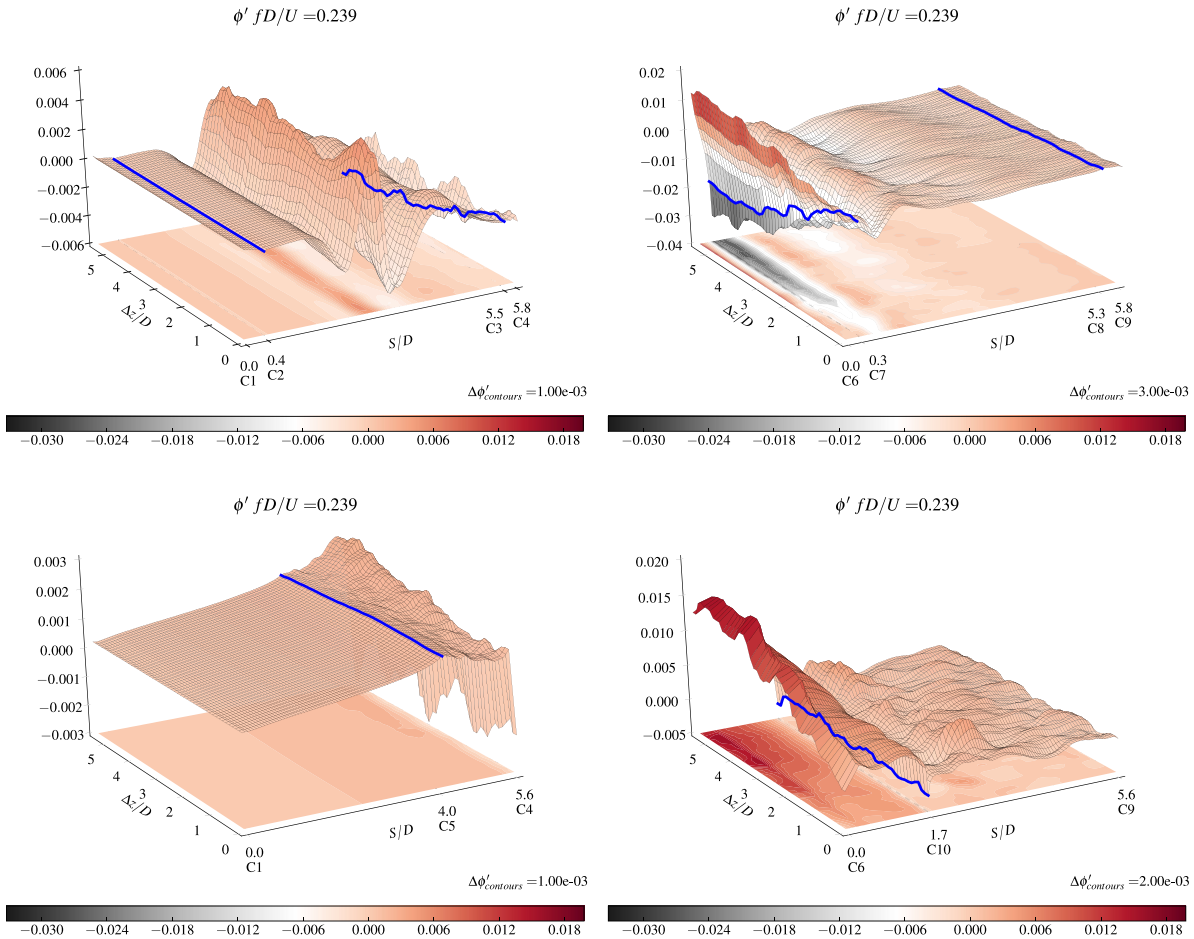

Fig. 20 First SPOD mode of the static simulation corresponding with the vortex shedding frequency. (The blue lines represent the position of the deck corners)

summation of the contribution of all the modes associated with that frequency. The difference between the first and second mode in the spectra is shaded in orange in the figure.

It can be appreciated that the overall SPOD spectrum for the static simulation presents a single main peak corresponding with the vortex shedding frequency (Fig. 19a). However, for the VIV two peaks are present (Fig. 19b), corresponding with the vortex shedding frequency, and the natural frequency of the system. Moreover, two super-harmonics related with the vortex shedding frequency are also identified, in agreement with the results obtained for the POD modes in Sect. 5.1.

According to Schmidt et al. [26], if the eigenvalues of the modes for a specific frequency are well separated among them, the travelling structures in the flow may be represented by the first mode associated to each particular frequency. In this application case, the first mode associated to a certain frequency, represents the pressure footprint of the travelling structures just mentioned.

In Fig. 20, the SPOD mode associated to the first eigenvalue at the frequency of vortex shedding for the static twin-box deck is depicted. It presents similarities with the first POD mode of the static simulation, as the main flow energy content is associated with vortex shedding.

For the VIV case, the modes of the two main frequency peaks in the spectra associated to the first eigenvalue at each frequency are reported in Fig. 21. The one corresponding with the vortex shedding

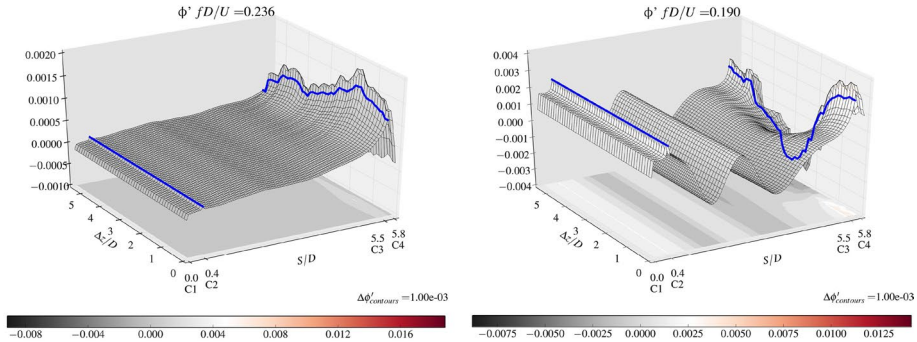

(a) Upper surfaces of the upwind box.

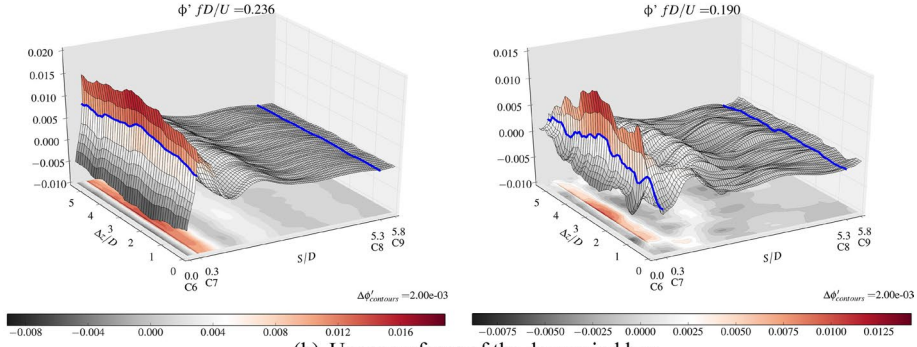

(b) Upper surfaces of the downwind box.

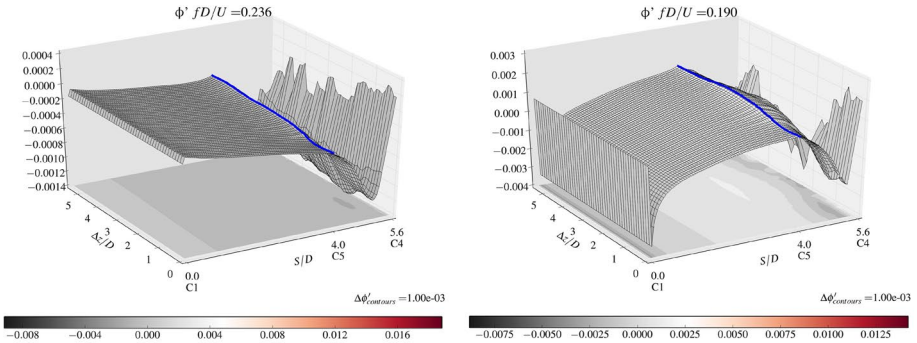

(c) Lower surfaces of the upwind box.

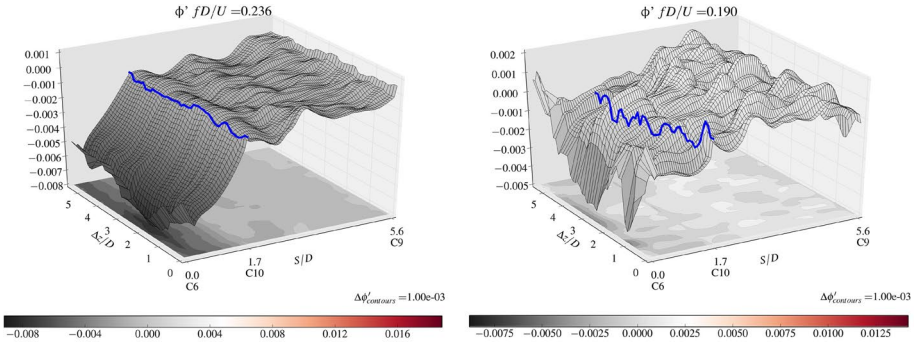

(d) Lower surfaces of the downwind box.

Fig. 21 SPOD modes of the VIV simulations corresponding with the main peak of the spectra (left column) and with the secondary one (right column). (The blue lines represent the position of the deck corners)

frequency ($fD/U = 0.236$) resembles the first POD mode of the VIV case (see Fig. 16), for which the main frequency is the one of the vortex shedding. On the other hand, the SPOD mode corresponding with the natural frequency of the system ($fD/U = 0.190$) does not compare in a straightforward manner as in the previous cases, presenting a combination of the features of both the second and third modes of the POD analysis.

Interestingly, for both the static and VIV cases, the SPOD mode shapes at the frequency of vortex shedding show amplitudes at the downwind box roughly one order of magnitude higher than at the upwind box. On the other hand the amplitudes are similar at the two boxes for the SPOD mode shape at the natural frequency of the system. This highlights the importance of the interactions between the vortices shed from the upwind box and the downwind box, both in the static and peak VIV response cases.

5.2.1 *Analysis of each individual box based on SPOD analysis*

In the previous section, the SPOD approach has been applied to analyse the pressure coefficient distributions over the two deck boxes, which enables the study of the general flow features around the deck. However, the aerodynamic response might be very different for each individual box, remarkably since the downwind box is fully immersed in the wake of the upwind box. To further analyse the flow aerodynamics over the deck, the SPOD analysis has been applied to the time-dependent pressure distribution acting on each individual box. The spectra obtained for the static simulation are presented in Fig. 22, meanwhile the results for the case undergoing heave oscillations at $U/(f_0 B) = 0.35$ are reported in Fig. 23. It can be seen how the peak frequencies are the same as in the global deck analysis.

For the static case, it can be noticed that the upwind box does not present a second super-harmonic vortex shedding peak (see Fig. 22a), meanwhile this second super-harmonic is clearly present in the downwind box (Fig. 22b), which shows the potential of the SPOD approach to deliver a better description of the complex flow features in this deck arrangement.

Moving now to the heave VIV excitation case, the second super-harmonic might be identified in both boxes, although this peak is very small at the upwind box (Fig. 23a). Moreover, it must be highlighted that the main frequency in the SPOD analysis of the upwind box is the one related with the natural heave

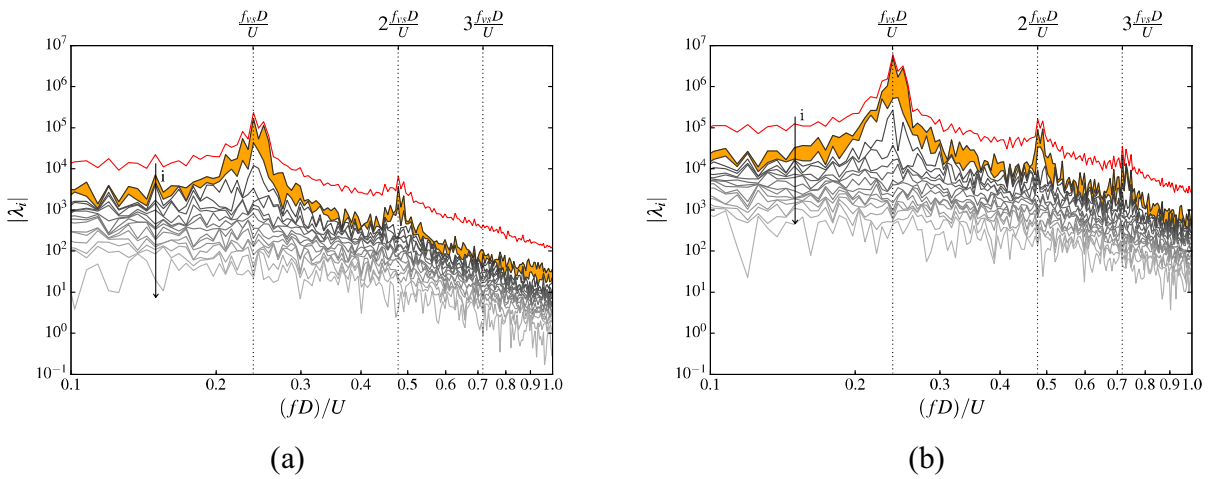

Fig. 22 Energy spectra from the SPOD modes of the static simulation: **a** upwind box and **b** downwind box. (λ_i is the eigenvalue of the i mode for each frequency. i increases in the direction of the arrow) (f_{vs} is the vortex shedding frequency. D is the height of the deck and U is the wind speed)

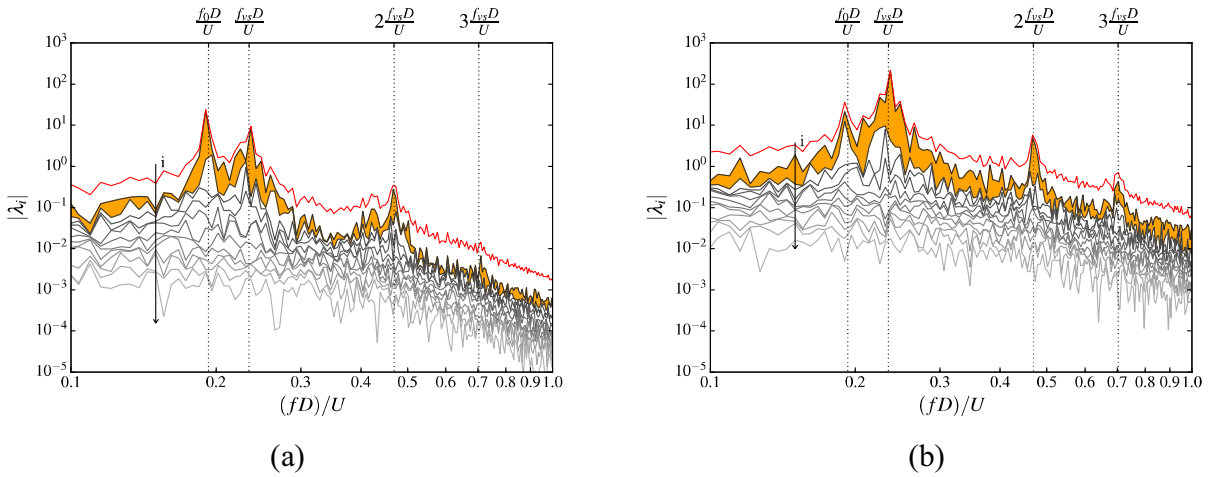

Fig. 23 Energy spectra from the SPOD modes of the VIV simulation: **a** upwind box and **b** downwind box. (λ_i is the eigenvalue of the i mode for each frequency. i increases in the direction of the arrow) (f_0 is the natural frequency of the heave system, f_{vs} is the vortex shedding frequency. D is the height of the deck and U is the wind speed)

frequency (Fig. 23a), in contrast with the main peak at vortex shedding frequency identified for the overall deck and the downwind box. Moreover, in Fig. 23, the spectrum peaks related with the natural frequency of the dynamical system are almost identical for each individual box, but the spectrum peak corresponding with vortex shedding is two orders of magnitude bigger relative to the upwind box, and one order of magnitude bigger than the natural frequency peak of the downwind box. Therefore, far more energy is transferred to the heave oscillation from the downwind box than from the upwind one, hence the oscillation is controlled by the downwind box. Furthermore, it is noticeable that the SPOD spectra for the downwind box (Figs. 22b and 23b) almost perfectly resemble the overall SPOD-based spectra for the complete deck in Fig. 19.

5.3 DMD modal analysis

Although the SPOD approach enables a deeper understanding about the frequency and energy content in the time-dependent pressure distributions acting on the deck, no information might be retrieved about their time evolution of the flow action on the deck. The DMD decomposition, provides modes containing a single frequency component, but also the damping associated with each mode [29], and enables, therefore, the study of the spatio-temporal evolution of the field under study [18]. In Fig. 24, the eigenvalues obtained for each mode are presented for the static and VIV cases. The dashed line represents a circumference of unitary radius (note the different scale in the coordinate axes in Fig. 24 causing the elliptical appearance), signalling the limit between decaying and diverging modes. According to Jovanovi et al. [14], the points inside the circumference are strongly damped, so these modes will only be important at the early stages of the time dependent process. It can be noticed how no points are located outside the dashed line, as the VIV phenomenon is a self-limited process [27] and no divergence of the heave oscillation will take place as time passes by. The DMD decomposition makes possible obtaining a spectrum that identifies the modes at the initial stages and the ones in the long term, after the flow has evolved over time.

In Fig. 25, the energy spectra of the static and VIV simulations for both the early and long-term stages are presented. It can be noticed how at the early stages multiple frequencies are present in the pressure field, with the maximum located at the vortex shedding frequency (Fig. 25a, c). On the other hand, when the modes have been damped, the range of frequencies contained in the pressure field has drastically decreased. For the static case, it is restricted only to the vortex shedding frequency. Nevertheless, for the peak VIV case, the mode corresponding with the natural frequency of the system has not vanished,

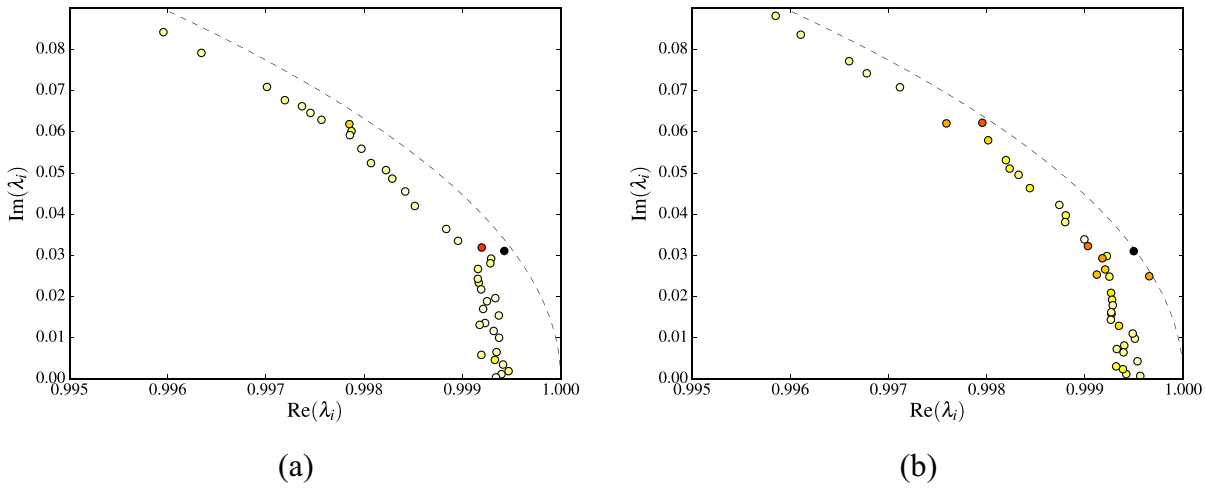

Fig. 24 Modes eigenvalues, the darker the colour of the circles, the higher the value of the energy spectra at the initial stage. **a** Static simulation and **b** VIV simulation

along with the vortex shedding frequency and the first of its super-harmonics. The amplitudes presented in Fig. 25 follow the definition given by Rosa Domingos [23], in which a_i is the projection of the mode φ_i with respect the first snapshot of the pressure field under study.

The main DMD mode of the static simulation, corresponding with the vortex shedding frequency is presented in Fig. 26. This mode resembles the first mode obtained from the POD analysis (Fig. 13), but in this case it has a single frequency component as in the SPOD method (see Fig. 20 for asserting the resemblance among modes). It may be noticed how the upper surfaces of the boxes are the ones showing higher oscillation in amplitude in the modes in the advection direction, associated with vortex build up and vortex detachment. This phenomenon can also be appreciated, but at a smaller scale, on the lower surfaces of the downwind box, associated with the weak vortex detached from them.

The DMD modes associated with the vortex shedding frequency and the natural frequency of the dynamic system for the peak VIV case are presented in Fig. 27. The mode amplitude at the vortex shedding frequency is reduced with respect to the mode of the static simulation, transferring this energy to the mode associated with the natural frequency of the heave oscillation system.

According to Luo et al. [18], the DMD modes, as the ones obtained in this study, would be representative of the macro-scale flow action on the deck, because they possess a high spatial coherence and contain a substantial part of the energy contained in the spectrum. In this case, we are seeing the effect of these flow structures over the pressure field around the deck. These macro-scale DMD modes are associated with large scale flow features, and hence they are related with the energy transferred by the flow approaching the deck, representing its spatio-temporal features [7] in vortex shedding and VIV.

The DMD approach also provides modal amplitudes roughly one order of magnitude higher over the downwind box relative to the upwind one for the

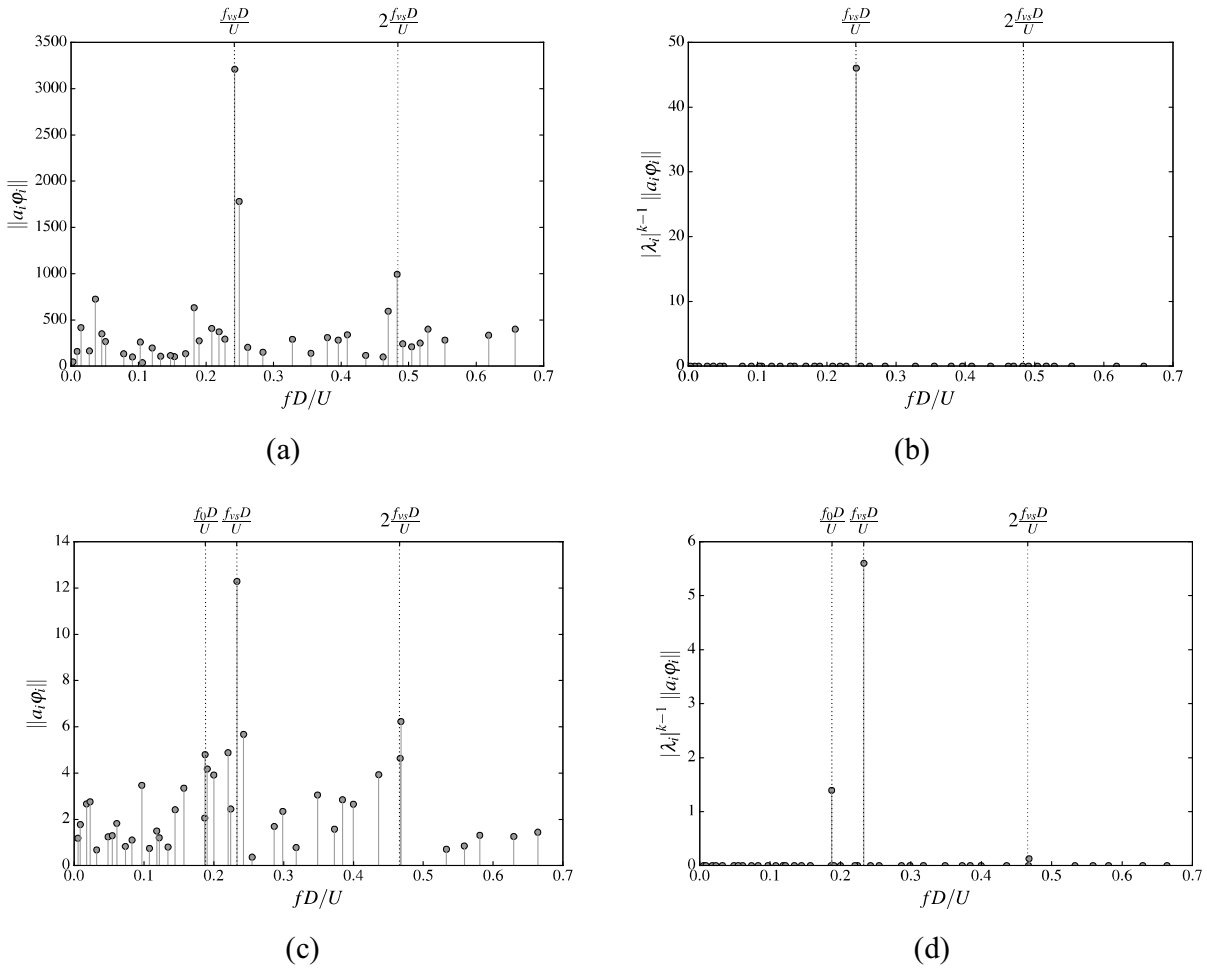

Fig. 25 Energy spectra from the DMD modes, for the static simulations: **a** initial stages and **b** evolved stages; and the VIV simulations: **c** initial stages and **d** evolved stages. (f_0 is the natural frequency of the heave system, f_{vs} is the vortex shedding frequency. D is the height of the deck and U is the wind speed)

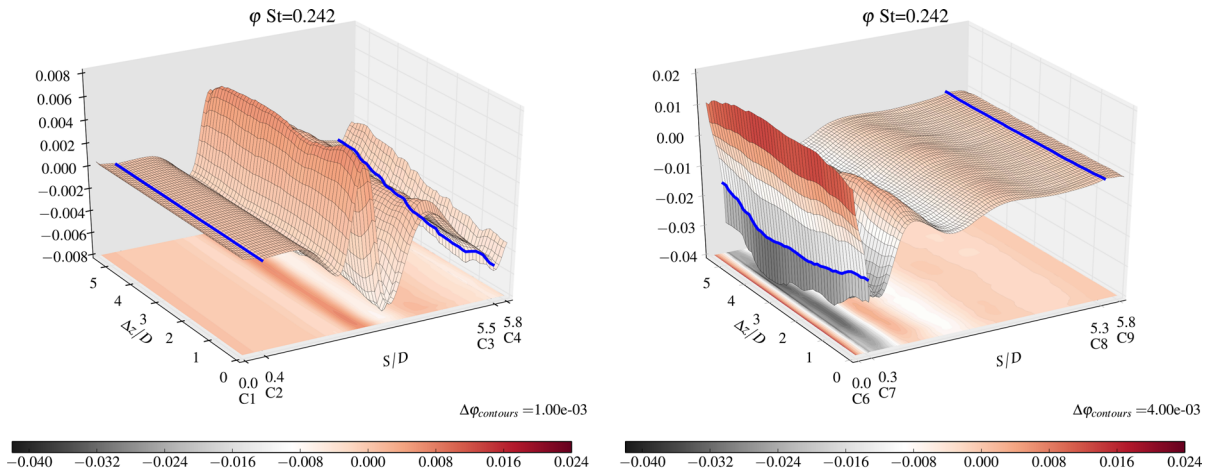

(a) Upper surfaces.

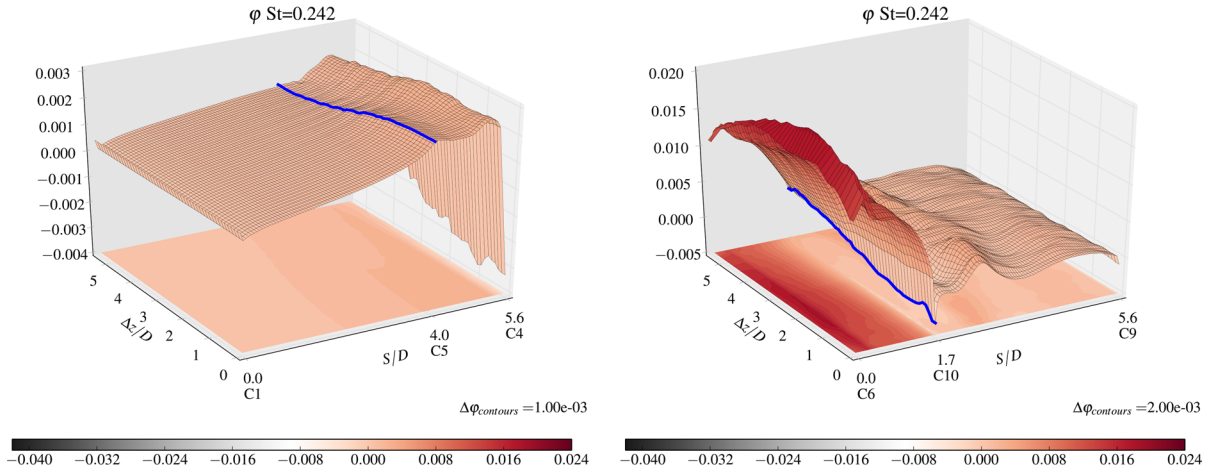

(b) Lower surfaces.

Fig. 26 DMD mode of the static simulation corresponding with the vortex shedding frequency. (The blue lines represent the position of the deck corners)

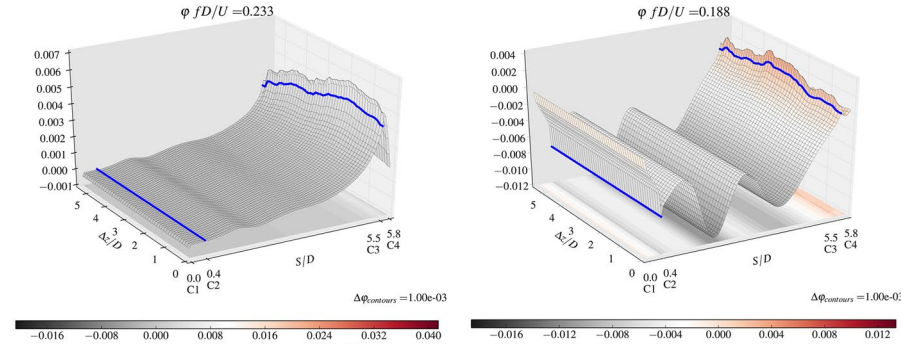

(a) Upper surfaces of the upwind box.

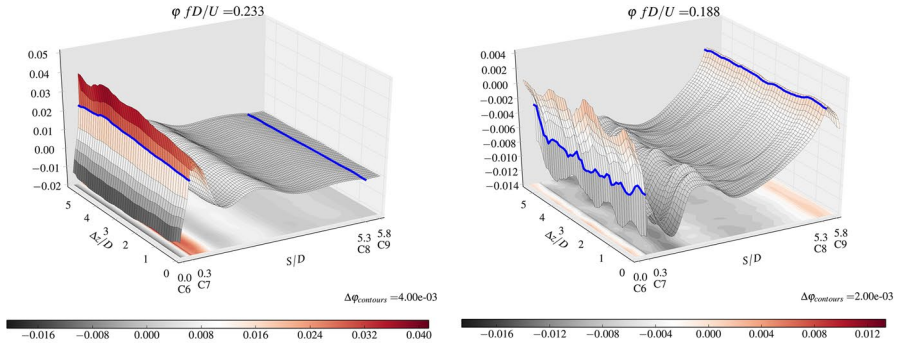

(b) Upper surfaces of the downwind box.

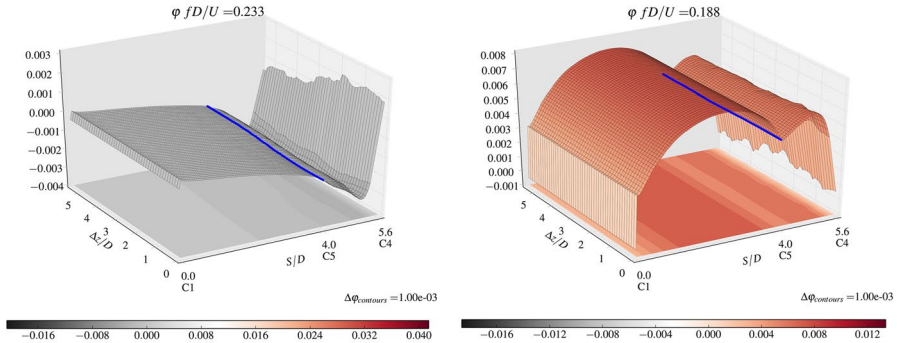

(c) Lower surfaces of the upwind box.

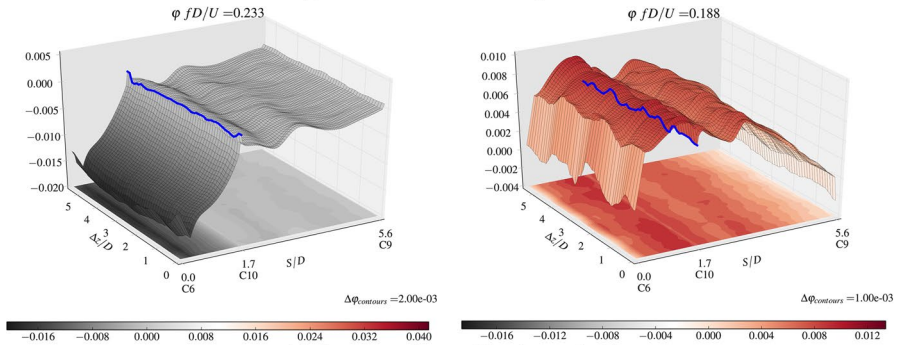

(d) Lower surfaces of the downwind box.

Fig. 27 DMD modes of the VIV simulations, related with the vortex shedding frequency (left column) and with the natural frequency of the system (right column). (The blue lines represent the position of the deck corners)

vortex shedding frequency. However for the natural frequency of the system in the VIV case, the amplitudes of the mode are similar. This is in agreement with the features described for the SPOD approach.

6 Conclusions

Twin box decks show complex flow features due to the interplay between the flow and the parallel boxes, being the gap distance between them a key parameter. This deck typology is prone to VIV, and in this CFD-based research, advanced modal techniques and correlation analyses have been applied aiming at deciphering the intricacies of the fluid–structure interaction.

The main findings and contributions of this work are:

- The assessment of the correlation of the time dependent force coefficients has permitted a better understanding about how the flow organisation impacts the magnitude of the flow forcing action. In the application case, this approach enabled to identify the differences in the flow around the static deck and the peak VIV response in heave.
- The application of three different modal analysis techniques has showcased the strong points of each one and the complementarity among them. Based on the extracted modal information, a better understanding about the complex interplay among the aerodynamic response of each box has been possible.
- Based upon the spectra obtained for the different modal decomposition techniques used, it has been demonstrated that the main frequencies governing the pressure field over the deck, correspond with the vortex shedding frequency for the static case and both, the vortex shedding frequency and the natural frequency of the one degree of freedom dynamical system for the VIV case. The most prominent peak for the overall deck at VIV is the one corresponding with the vortex shedding frequency, feeding energy to the system in order to sustain the oscillations.
- Moreover, the analysis of the SPOD spectra for each individual box, has permitted to identify the time-dependent pressure distributions around the downwind box as the ones controlling the VIV phenomenon. This is consistent with the accepted knowledge about the importance of the gap distance in the VIV response of the twin-box decks, taken into account that the flow around the upwind box is weakly affected by the gap distance for medium to large slots.
- The analysis of the DMD modes provided an explanation for the self-limiting characteristic of VIV and confirmed the critical role played by the downwind box, in agreement with the SPOD outputs.

Finally, the successful application of these modal methods enables the extension of this piece of research in the development of reduced order models (ROM) for VIV excitation of twin-box decks in future research efforts.

Acknowledgements The computations have been carried out in the computer cluster Breogán and in the Galicia Supercomputing Centre (CESGA). The authors also would like to thank the organizing committee of the 18th OpenFOAM Workshop for all the support provided for success of the Conference, and in the organization of this special issue.

Author contributions Conceptualisation: Antonio J. Álvarez, Félix Nieto Methodology: Antonio J. Álvarez, Félix Nieto Formal analysis and investigation: Antonio J. Álvarez Writing - original draft preparation: Antonio J. Álvarez, Félix Nieto Writing - review and editing: Antonio J. Álvarez, Félix Nieto Funding acquisition: Antonio J. Álvarez, Félix Nieto Resources: Félix Nieto Supervision: Félix Nieto

Funding Open Access funding provided thanks to the CRUE-CSIC agreement with Springer Nature. This research has been funded by the Spanish Ministry of Economy and Competitiveness in the frame of the research project with reference PID2019-110786GB-I00 and the Galician regional government with references ED431C 2021/33. The first author has also been funded by the Galician regional government through a postdoctoral scholarship with reference ED481B-2021-133. Funding for open access charge: Universidade da Coruña/CISUG.

Data availability The data associated with this piece of research would be made available upon reasonable request, as this piece of research is part of a still ongoing research project.

Declarations

Conflict of interest The authors declare no competing interests.

Ethical approval Not applicable.

References

1. Álvarez AJ, Nieto F, Hernándex S (2022) Computational simulation of the vortex-induced vibration of a twin-box deck. In: Proceedings of the 8th European-African conference on wind engineering, Bucharest, Romania
2. Álvarez AJ, Nieto F, Kwok KCS, Hernández S (2021) A computational study on the aerodynamics of a twin-box bridge with a focus on the spanwise features. J Wind Eng Ind Aerodyn 209:104465. https://doi.org/10.1016/j.jweia.2020.104465
3. Álvarez AJ, Nieto F, Nguyen DT, Owen J, Hernández S (2019) 3D LES simulations of a static and vertically free-to-oscillate 4:1 rectangular cylinder: effects of the grid resolution. J Wind Eng Ind Aerodyn 192:31–44. https://doi.org/10.1016/j.jweia.2019.06.012
4. Álvarez AJ, Nieto F, Hernándex S (2021) Verification approaches for the 3D static LES simulations of the Stonecutters bridge deck. In: Proceedings of the 11th International Conference on Advances in Fluid Dynamics with emphasis on Multiphase and Complex Flow, Southampton, UK. https://doi.org/10.2495/MPF210101
5. Blocken B (2014) 50 years of computational wind engineering: past, present and future. J Wind Eng Ind Aerodyn 129:69–102. https://doi.org/10.1016/j.jweia.2014.03.008
6. Bruno L, Fransos D, Coste N, Bosco A (2010) 3D flow around a rectangular cylinder: a computational study. J Wind Eng Ind Aerodyn 98:263–276. https://doi.org/10.1016/j.jweia.2009.10.005
7. Carassale L (2012) Analysis of aerodynamic pressure measurement by dynamic coherent structures. In: Porbabilistic engineering mechanics, vol 28, pp 66–74. https://doi.org/10.1016/j.probengmech.2011.08.010
8. Celik IB, Ghia U, Roache PJ, Freitas CJ, Coleman H, Raad PE (2008) Procedure for estimation and reporting of uncertainty due to discretization in CFD applications. Journal of Fluids Engineering, 130:078001–1–4. https://doi.org/10.1115/1.2960953
9. de Miranda S, Patruno L, Ricci M, Ubertini F (2015) Numerical study of a twin box bridge deck with increasing gap ratio by using RANS and LES approaches. Eng Struct 99:546–558. https://doi.org/10.1016/j.engstruct.2015.05.017
10. Fransos D, Bruno L (2010) Edge degree-of-sharpness and free-stream turbulence scale effects on the aerodynamics of a bridge deck. J Wind Eng Ind Aerodyn 98:661–671. https://doi.org/10.1016/j.jweia.2010.06.008
11. Geuzaine C, Remacle JF (2009) Gmsh: a three-dimensional finite element mesh generator with built-in pre- and post-processing facilities. Int J Numer Meth Eng 79(11):1309–1331. https://doi.org/10.1002/nme.2579
12. Greenshields CJ (2017) User guide. Version 5.0. OpenFOAM Foundation Ltd
13. Holmes P, Lumley JL, Berkooz G (1996) Turbulence, coherent structures, dynamical systems and symmetry. Cambridge University Press, Cambridge. https://doi.org/10.1017/CBO9780511622700
14. Jovanovi MR, Schmid PJ, Nichols JW (2014) Sparsity-promoting dynamic mode decomposition. Phys Fluids 26(3):024103. https://doi.org/10.48550/arXiv.1309.4165
15. Kareem A (2020) Emerging frontiers in wind engineering: computing, stochastics, machine learning and beyond. J Wind Eng Ind Aerodyn 206:104320. https://doi.org/10.1016/j.jweia.2020.104320
16. Kwok KCS, Qin XR, Fok CH, Hitchcock PA (2012) Wind-induced pressures around a sectional twin-deck bridge model: effects of gap-width on the aerodynamic forces and vortex shedding mechanisms. J Wind Eng Ind Aerodyn 110:50–61. https://doi.org/10.1016/j.jweia.2012.07.010
17. Larsen A, Savage M, Lafreniere A, Hui MCH, Larsen SV (2008) Investigation of vortex response of a twin box bridge section at high and low Reynolds numbers. J Wind Eng Ind Aerodyn 96:934–944. https://doi.org/10.1016/j.jweia.2007.06.020
18. Luo X, Kareem A (2021) Dynamic mode decomposition of random pressure fields over bluff bodies. J Eng Mech 147(4):04021007. https://doi.org/10.1061/(ASCE)EM.1943-7889.0001904
19. Oberleithner K, Rukes L, Soria J (2014) Mean flow stability analysis of oscillating jet experiments. J Fluid Mech 757:1–32. https://doi.org/10.1017/jfm.2014.472
20. Ravindran SS (2000) A reduced order approach for optimal control of fluids using proper orthogonal decomposition. Int J Numer Methods Fluids 38(10):425–448. https://doi.org/10.1002/1097-0363(20001115)34:5%3c425::AID-FLD67%3e3.0.CO;2-W
21. Ricciardelli F (2010) Effects of the vibration regime on the spanwise correlation of the aerodynamic forces on a 5:1 rectangular cylinder. J Wind Eng Ind Aerodyn 98:215–225. https://doi.org/10.1016/j.jweia.2009.10.017
22. Rowley CW (2005) Model reduction for fluids, using balanced proper orthogonal decomposition. Int J Bifurcat Chaos Appl Sci Eng 15(3):997–1013. https://doi.org/10.1142/S0218127405012429
23. Rosa Domingos JM (2014) Dynamic mode decomposition method—application to the Earth's liquid core. MA thesis. Coimbra, Portugal: Universidade de Coimbra
24. Sarkic A, Höffer R, Stanko B (2015) Numerical simulations and experimental validations of force coefficients and flutter derivatives of a bridge deck. J Wind Eng Ind Aerodyn 144:172–182. https://doi.org/10.1016/j.jweia.2015.04.017

25. Smagorinsky J (1963) General circulation experiments with the primitives equations I: the basic experiment. Month Weath Rev 3(91):99–165. https://doi.org/10.1175/1520-0493(1963)091%3c0099:GCEWTP%3e2.3.CO;2
26. Schmidt OT, Colonius T (2020) Guide to spectral proper orthogonal decomposition. AIAA J 58(3):1023–1033. https://doi.org/10.2514/1.J058809
27. Simiu E, Scanlan RH (1986) Wind effects on structures, 2nd edn. Wiley, New York. https://doi.org/10.1002/9781119375890
28. Taira K, Brunton SL, Dawson STM, Rowley CW, Colonius T, McKeon BJ, Schmidt O, Gordeyev S, Theofilis V, Ukeiley LS (2017) Modal analysis of fluid flows: an overwiew. AIAA J 55(12):4013–4041. https://doi.org/10.2514/1.J056060
29. Tu JH, Rowley CW, Luchtenburg DM, Brunton SL, Kutz JN (2014) On dynamic mode decomposition: theory and applications. J Comput Dyn 1(2):391–421
30. Wilcox DC (2012) Basic fluid mecanics, 5th edn. DCW Industries, La Cañada